

# Highlights

## **In-Season Crop Progress in Unsurveyed Regions using Networks Trained on Synthetic Data**

George Worrall, Jasmeet Judge  
Center for Remote Sensing  
Agricultural and Biological Engineering Department  
University of Florida

- Satellite data are used in neural networks (NN) for crop progress estimation (CPE)
- Current CPE methods require survey data and cannot be used in unsurveyed regions (UR)
- Linked weather-crop-optical radiative transfer models provide synthetic data for UR
- NNs can be trained on synthetic data and real CP data from surveyed regions (SR)
- NNs trained on simultaneously on CP from SR and synthetic data improves CPE in UR

# In-Season Crop Progress in Unsurveyed Regions using Networks Trained on Synthetic Data

George Worrall, Jasmeet Judge  
Center for Remote Sensing  
Agricultural and Biological Engineering Department  
University of Florida

---

## Abstract

Many commodity crops have growth stages during which they are particularly vulnerable to stress-induced yield loss. In-season crop progress information is useful for quantifying crop risk, and satellite remote sensing (RS) can be used to track progress at regional scales. At present, all existing RS-based crop progress estimation (CPE) methods which target crop-specific stages rely on ground truth data for training/calibration. Such data are collected via field trials or surveys. This reliance on ground survey data confines CPE methods to surveyed regions, limiting their utility. In this study, a new method is developed for conducting RS-based in-season CPE in unsurveyed regions by combining data from surveyed regions with synthetic crop progress data generated for an unsurveyed region of interest. Corn-growing zones in Argentina were used as surrogate ‘unsurveyed’ regions. These zones have climates and dual planting systems which differ the single planting system in the US Midwest – the surveyed region in this study. Existing weather generation, crop growth, and optical radiative transfer models were linked to produce synthetic weather, crop progress, and canopy reflectance data. These data mimic weather, cultivars, and cropping practices in the unsurveyed region. A neural network (NN) method based upon bi-directional Long Short-Term Memory was trained separately on surveyed data, synthetic data, and two different combinations of surveyed and synthetic data. In the absence of real validation data in unsurveyed regions, a stopping criterion was developed which uses the weighted divergence of surveyed and synthetic data validation loss.  $F_1$  score was modified to measure CPE accuracy when trained the NN was trained on each data combination, with scores based on over- and under-estimates of crop progress throughout the season. Including synthetic data during training improved performance in 9 out of 11 corn-growing zones in Argentina. Net  $F_1$  scores across all crop progress stages increased by 8.7% when trained on a combination of surveyed region and synthetic data, and overall performance was only 21% lower than the best case scenario, when the NN was trained on surveyed data and applied in the US Midwest. Performance gain from synthetic data was greatest in zones with dual planting windows, while the inclusion of surveyed region data from the US Midwest helped mitigate NN sensitivity to noise in NDVI data. Overall results suggest in-season CPE in other unsurveyed regions may be possible with increased quantity and variety of synthetic crop progress data.

*Keywords:* Crop progress, deep learning, long short-term memory, crop phenology, physics-guided machine learning, synthetic training data

---

## 1. Introduction

Many commodity crops have critical growth stages during which they are at an increased risk of stress-induced yield loss, such as silking in corn and pod-fill in soybean (Claassen and Shaw, 1970; Doss et al., 1974). Extreme weather events are expected to disrupt global food supply with increased frequency (Ray et al., 2015; Mehrabi and Ramankutty, 2019), and knowledge of the timing of crop growth stages in major growing regions is vital to accurately anticipate and quantify potential yield loss. Tracking crop growth stage progression, hereafter crop progress, is commonly done using ground surveyors. This task is laborious and requires widespread reporting infrastructure to produce the accurate and timely data. For example, in the US, the USDA coordinates weekly Crop Progress and Condition (CPR) reporting from over 5000 surveyors during the growing season (USDA National Agricultural Statistics Service, b). However, many major exporting countries do not have publicly available crop progress data or surveys. Growers and grain market participants are then less informed about the present vulnerability of a region’s crop to adverse weather, which can lead to significant revisions to production estimates by government institutions when effects become apparent late in a growing season, (e.g. Colussi and Schnitkey (2021)). For many regions, their geographical size and lack of survey infrastructure prevent the collection of comprehensive crop progress data.

In these unsurveyed regions, remote sensing (RS) observations may be used to estimate crop progress. The global coverage and frequent revisit times of modern earth-observing satellite platforms can provide cost-effective assessments of crop progress timing and may alleviate the need for ground survey infrastructure. Existing RS-based crop progress estimation (CPE) methods use observed crop canopy reflectances from a target growing region to derive relationships between vegetation indices (VI) such as normalized difference vegetation index (NDVI) and crop progress (Gao and Zhang, 2021). Many studies relate full-season VI curves to crop progress timing, such as Diao (2020); Diao et al. (2021); Seo et al. (2019). These

methods are useful for post-season analysis, but timely and frequent in-season estimates of crop progress are needed to quantify crop risk. This is because many critical growth stages in commodity crops, such as silking in corn (Claassen and Shaw, 1970), last under two weeks. To meet these requirements, RS-based in-season studies have sought to produce actionable CPE through trend-based approaches, which use momentum indicators and thresholding to produce estimates for events such as emergence (Gao et al., 2020a) and cover crop termination (Gao et al., 2020b). These approaches, however, utilize region-specific, user-defined parameters and do not target all growth stages. In addition, relationships between trend-based reference points such as ‘green-up’ and ‘maximum greenness’ and crop-specific growth stages is known to vary by method used (Liu et al., 2018; Gao and Zhang, 2021).

Machine learning (ML) techniques, such as Hidden Markov Models (HMM) (Shen et al., 2013) and Parametric Empirical Bayes (PEB) (Ghamghami et al., 2020), have been used to develop in-season CPE methods that can derive crop progress across all stages. These methods use historical crop progress as priors and estimate stage transition probabilities directly from RS and weather observations. However, both HMM and PEB rely on expectation maximization, which is sensitive to random weight initialization, and cannot derive higher order relationships between variables that are possible with contemporary ML techniques such as neural networks (NNs). Recently, Worrall et al. (2021) found that Long Short-Term Memory (LSTM), an NN architecture widely used in time series analysis (Zeyer et al., 2019; Cheng et al., 2019; Song et al., 2020), could be used to combine RS-based Fraction of Photosynthetically Active Radiation (FPAR) data with soil and weather conditions for in-season CPE. Worrall et al. (2021) found that LSTM-based in-season CPE produced 43% higher average Nash-Sutcliffe Efficiency across all stages than the HMM method from Shen et al. (2013). NN-based in-season CPE has shown further improvement when guided by biophysical crop models. For example, Worrall et al. (2022) found that growth stage and water stress-related information from biophysical crop growth model simulations increased overall in-season CPE accuracy, particularly during seasons with abnormal temperatures and higher

rainfall. Despite these recent advances in RS-based CPE, all existing methods still require ground truth crop progress data for calibration and/or training, limiting their application to regions where such data are available (Seo et al., 2019; Diao et al., 2021; Worrall et al., 2022).

In unsurveyed regions, studies have mapped RS-derived land surface phenology, such as ‘start-of-season’ and ‘end-of-season’ (Vintrou et al., 2014; Duncan et al., 2015). However, crop progress in unsurveyed regions cannot be estimated from these points because ground survey data is required to derive crop-specific stage estimates from land surface phenology (Seo et al., 2019; Diao, 2020), which are known to change based on the target crop, method used, and region of application (Liu et al., 2018; Gao and Zhang, 2021). To date, there are no RS-based methods that produce in-season CPE without ground survey data.

RS-based CPE in unsurveyed regions is difficult because there are no labeled data. In agricultural RS, crop mapping and yield estimation studies have addressed labeled data sparsity using transfer learning (Nowakowski et al., 2021; Luo et al., 2022; Khaki et al., 2021), which involves pre-training an NN on a large, often unrelated dataset before fine-tuning it on limited available labeled data. Given the success of transfer learning in these studies, it may be possible to leverage information from labeled data in surveyed regions, such as the US, to train NN-based methods and apply them to unsurveyed regions for in-season CPE. However, without any fine-tuning examples of cropping practices, cultivar choices, and climate in unsurveyed regions, their transferability may be limited.

Another approach to mitigating data sparsity is to use generative methods to provide additional, synthetic training examples. Generation of synthetic examples is common in RS-based scene classification, where manual partitioning and labeling of scenes is labor intensive (Cheng et al., 2020). A common generative method used in scene classification is Generative Adversarial Networks (GANs), which produce additional, synthetic examples of class-specific patterns from a limited number of hand-labeled samples (Qian et al., 2020; Han et al., 2020). GANs are effective for image recognition tasks, but they require some labeled data to

learn by example, which are not available for unsurveyed regions. Therefore, any generative method used to produce synthetic crop progress data must contain the underlying physical relationships among weather, crop growth and development, and observed reflectances that are present in real data without the need for labeled examples.

Physically-based models for weather generation, crop growth, and canopy reflectances are widely used in agriculture and RS studies. Studies in agronomy often utilize stochastic weather generators to assess the impacts of different climate scenarios on crop production (Semenov and Barrow, 1997; Apipattanavis et al., 2010; Supit et al., 2012). Some studies calibrate biophysical crop models, driven by soil and weather data, to produce in-season yield estimates (Archontoulis et al., 2020; Akhavizadegan et al., 2021). In RS, optical radiative transfer models (RTMs), which simulate canopy reflectances at visible and infra-red wavelengths from plant structure and leaf pigment concentrations, are often inverted to retrieve estimates of Leaf Area Index (LAI) and chlorophyll content (Duan et al., 2014; Jay et al., 2017). When these weather, crop, and RS models are linked, they can produce synthetic data that emulate real spatio-temporal patterns in agricultural production and their optical signatures, as observed from RS platforms. For example, Lobell et al. (2015) used the APSIM crop model and LAI-VI relationships to calibrate an RS-based regression model for post-season yield estimation. There is precedent in the literature for using historical weather, mechanistic crop models, and RTMs to generate data for synthetic studies, such as soil moisture downscaling using microwaves (Chakrabarti et al., 2015) and forest biomass estimation (Fassnacht et al., 2018). However, to our knowledge, synthetic data generated from linked weather-crop-RTM models have not been leveraged to train NNs for application in areas without ground truth data.

The goal of this study is to explore how well synthetic data may mitigate the need for ground survey data to produce in-season crop progress estimates in unsurveyed regions. In this study, domain-specific models from meteorology, agronomy, and optical RS are linked to generate synthetic crop progress data. An NN-based RS CPE method is trained on both

this synthetic data and observed data from surveyed regions in the US, then applied to CPE in unsurveyed regions. To assess the value of including synthetic crop progress data in unsurveyed region CPE, we investigated the performance of the NN-based method when it was trained solely on surveyed region data from the US. Specifically, the objectives of this study are to (1) implement a linked weather generator-crop model-RTM framework that can produce synthetic examples of crop progress data for an unsurveyed region, (2) investigate the impact of exposure to synthetic crop progress data during training on NN-based in-season CPE accuracy in unsurveyed regions, and (3) assess how NN-based CPE performance is affected by varied cropping practices in unsurveyed regions.

## 2. Study Regions and Datasets

Argentina represented the ‘unsurveyed’ region in this study as it is one of the few countries, other than the US, with publicly available weekly crop progress data that could be used for evaluation of the NN-based method. The states of Iowa and Illinois in the US Midwest represented the ‘surveyed’ region. Both Argentina and the US are large exporters of staple crops such as corn and wheat. Corn, the second largest crop by global production, was used as the example crop (FAO, 2022). In Argentina, the majority of corn is grown in a two-crop system, in which an early and late-season crop are planted September-November and December-January, respectively. The Argentine Bolsa de Cereales (BdC) defines 13 growing zones, of which 11 are surveyed for corn production (see Figure 1). Nine out of these 11 zones grow both an early and a late corn crop (see Table 1 and Figure 2), which creates bimodal corn crop progress across a growing season. Additionally, temperate climates in the central zones allows for near-year round production, including winter-summer double cropping and post-season cover crops. In contrast, in the US Midwest, corn is grown in a single crop system from April to November, with an April-May planting window in each of the eighteen USDA-defined districts in Iowa and Illinois (see Figure 3). The differences in corn cultivation between Argentina and the US Midwest make Argentina an excellent disparate ‘unsurveyed’ test case for assessing the impacts of varied climate and cropping practices on

the performance of the in-season CPE methods developed in this study.

### 2.1. Datasets

This study used crop progress data from ground surveys, satellite RS and meteorological data to monitor corn crop progress, and soil datasets to parameterize biophysical model simulations.

#### 2.1.1. Crop Progress Data

In Argentina, weekly crop progress data is collected by both ground surveys and telephone surveys for each zone by the BdC for both the early and late season corn crops (Departamento de Estimaciones Agrícolas, 2020). Growth stages recorded by the BdC include, expansión foliar (leaf expansion), panojamiento (tasseling), floración femenina (silking), grano pastoso (dough), madurez fisiológica (mature), and cosecha (harvested). Argentine growing seasons traverse the new year, and crop progress reports can span September to September for zones in which the climate is favorable for year-round production. In this study, crop progress data for the Argentine growing seasons of 2019/20 and 2020/21 were *only used for evaluation of the in-season CPE method*, and the NN-based CPE method was never exposed to real Argentine crop progress data during NN development and hyperparameter selection. In the US Midwest, crop progress data for corn is collected weekly by ground surveyors from the USDA at Agricultural Statistical District, hereafter district, level throughout the growing season (USDA National Agricultural Statistics Service, b). Stages recorded include planting, emerged, silking, dough, dent, mature, and harvested. Only crop progress data from the US Midwest growing seasons for years 2003–2020 and generated synthetic data for Argentina were used to train the NN-based in-season CPE method.

#### 2.1.2. Remote Sensing and Meteorological Data

Table 2 shows the remotely sensed data used as inputs to the NN-based CPE method, their resolutions and pre-processing. In this study, crop cover maps at 30 m of Argentina (de Aballeyra et al., 2020) for the 2019/20 and 2020/21 seasons and of the US (USDA Ag Data Commons, 2021) for the 2003–2020 seasons were used to identify corn pixels. Crop



maps were upscaled to 250 m using pixel averaging to match the resolution of the MODIS NDVI product. All pixels that contained < 90% corn cover were masked and the NDVI values from MODIS observations for each corn pixel were linearly interpolated to produce daily time series values for the pixel. These time series were then collated into histograms of daily NDVI values across each district/zone, with 20 histogram bins in the range 0 to 1. Negative NDVI values were set to 0.

Daily maximum and minimum air temperatures were used to form daily growing degree day (GDD) values for each district/zone, where GDD is calculated as

$$GDD = \begin{cases} \frac{T_{max}+T_{min}}{2} - T_{base}, & \text{if } \frac{T_{max}+T_{min}}{2} \geq T_{base} \\ 0, & \text{otherwise} \end{cases}$$

with  $T_{max}$  as the lesser of the daily maximum temperature and 34°C,  $T_{base} = 8^\circ\text{C}$ , and  $T_{min}$  as the daily minimum temperature. GDD is a common measure used to model the effects of temperature on crop growth and development. GDD time series for each corn pixel were aggregated into daily histograms with 27 bins, ranging from 0 to 26°C.

Histograms of NDVI and GDD time series for each district/zone began two weeks before the first historical planting date for that region. Figure 4 shows example of district/zone-level time series of NDVI and GDD for Northwest Iowa and Zone V. As shown in the figure, the NDVI values in Zone V exhibit two distinct peaks caused by the dual planting windows.

### 2.1.3. Soil Data

Soil reflectance spectra samples and spatial data on soil physical properties were used to generate synthetic data. The soil properties dataset used to run the biophysical crop model simulations at 10 km resolution for each corn growing zone within Argentina was a global, pre-formatted soil database derived from SoilGrids (Hengl et al., 2017) and HarvestChoice 27 (Koo and Dimes, 2013) produced by Han et al. (2019). This dataset contained gridded texture, bulk density, drainage rate, root growth factor, soil organic carbon, and saturated hydraulic conductivity of soils to a depth 2 m at a spatial resolution of 10 km.

Soil reflectance data at wavelengths from 400 nm to 2500 nm at 1 nm spectral resolution were acquired from the NASA Ecosystem Spaceborne Thermal Radiometer Experiment on Space Station (ECOSTRESS) spectral library (Meerdink et al., 2019). Surface soil properties from each 10 km grid within Argentina were matched to one of the 69 ECOSTRESS soil samples based on texture. Soil reflectance data from that sample were then used to simulate the soil component of synthetic optical reflectance for that grid.

### 3. Methodology

#### 3.1. Network Architecture

The NN structure used in this study was based upon Long Short-Term Memory (LSTM), a network architecture which has been used in agricultural RS for yield prediction (Schwalbert et al., 2020), crop mapping (Kerner et al., 2022), and in-season CPE (Worrall et al., 2021). In this study, we used a simple, two-stacked bi-directional LSTM structure, with the final hidden states of each LSTM layer fed into a single fully connected layer to produce crop progress estimates, as shown in Figure 5. LSTM layers each had 128 memory cells and the fully connected layer had 6 nodes.

The network used district/zone-level histograms of time series NDVI and GDD to estimate the crop progress distribution for each week,  $w$ , during the season. Histograms were masked beyond week  $w$  to simulate in-season estimation and prevent look ahead bias. Kulbeck-Leibler divergence was used for network loss, defined as:

$$D_{KL}(P||Q) = \sum_{x \in X} P(x) \log \left( \frac{P(x)}{Q(x)} \right) \quad (1)$$

where here  $P(x)$  and  $Q(x)$  are estimated and actual crop progress on week  $w$ . Each week’s crop progress was treated as a separate target, and a softmax output layer was used to ensure estimates across all stages for a given week summed to 100%.

#### 3.2. Synthetic Data Generation

Three models were linked to generate synthetic crop progress data on a 10 km grid within each of the 11 corn-growing zones in Argentina. These were a spatial version of the

Richardson-type stochastic weather generator (SWG), as proposed by Wilks (1998, 1999), the CSM-IXIM corn model from the Decision Support System for Agro-technology Transfer (DSSAT) crop model suite (Lizaso et al., 2011), and the PROSAIL-style RTM Soil-Plant-Atmosphere Radiative Transfer (SPART) model (Yang et al., 2020).

### 3.2.1. Spatial SWG

The spatial SWG is a generative weather model that produces spatially correlated precipitation, maximum and minimum temperature, and solar radiation data at daily time steps. The SWG typically uses historical weather data from weather stations in a target region to produce synthetic weather data which preserves both monthly mean, variance, and inter-annual variability of weather variables for individual stations as well as historical correlations between stations.

In the SWG, precipitation occurrence is modeled as a first order Markov chain and precipitation amount is modeled as a dual-exponential distribution of the form,

$$f[r(k)] = \frac{\alpha}{\beta_1(k)} \exp\left[\frac{-r(k)}{\beta_1(k)}\right] + \frac{1 - \alpha}{\beta_2(k)} \exp\left[\frac{-r(k)}{\beta_2(k)}\right]$$

where  $\alpha$  is the mixing parameter and  $\beta_1$ , and  $\beta_2$  are distribution parameters for weather station  $k$ . Daily solar radiation and maximum and minimum temperatures are generated using a first-order multi-variate autoregressive model

$$z_t = [\Phi]z_{t-1} + [B]e_t \tag{2}$$

where  $z_t$  is a vector of the residuals of solar radiation and maximum and minimum temperatures,  $\Phi$  is a  $3 \times 3$  matrix of autoregressive parameters, and  $B$  is a  $3 \times 3$  matrix of coefficients which multiply the standard Gaussian random numbers in  $e_t$  that drive the model. Autoregressive parameters and correlations between variables are calculated at each station for each month of the year, with different parameters fit for wet and dry days. The SWG generates spatially correlated weather data by using historical correlations between weather at different stations to condition a stream of random numbers which drive weather genera-

tion at individual station models. Inputs to the SWG are shown in Table 3 and the SWG implementation used in this study is available on GitHub (Worrall, 2022).

In order to produce synthetic crop progress data which retains the spatial correlations present in real crop progress, synthetic weather used to drive the linked crop model-RTM (see Figure 6) in a zone must be spatially correlated. In this study, zone borders acted as synthetic data generation boundaries, and the SWG was calibrated on historical weather data from within each zone. NASA POWER 0.5 deg gridded weather pixels were used as weather stations, with the weather archive from each of these pixels (1984–2022) used as SWG calibration data (NASA Langley Research Center). Individual station parameters for precipitation,  $\alpha$ ,  $\beta_1$ , and  $\beta_2$ , were derived for each NASA POWER weather pixel using maximum likelihood estimation, and spatial correlations between pixels within a zone were identified following the method from Wilks (1999). The SWG was used to generate 100 years of synthetic gridded weather data for each zone for 99 full growing seasons. GDDs for each generated synthetic weather pixel were calculated using simulated maximum and minimum temperatures, then aggregated to zone level following the method outlined in Section 2.1.2. Synthetic precipitation, solar radiation, maximum and minimum temperature data from each 0.5 deg weather pixel with a zone were used to drive DSSAT IXIM crop model simulations at 10 km, as shown in Figure 6.

### *3.2.2. CSM-IXIM*

Crop model simulations were conducted at 10 km resolution within each zone using the CSM-IXIM maize crop model (hereafter, IXIM) within DSSAT, a crop modeling suite that simulates crop growth, phenological progression, and yield of different crops (Jones et al., 2003). IXIM is a corn model that was developed by Lizaso et al. (2011) and is based upon the CERES-Maize model (Jones et al., 1983). The model inputs include soil (from Section 2.1.3) and weather conditions (from Section 3.2.1), as shown in Table 3, along with eight genetic and phenotypic parameters describing corn cultivars. The fundamental driver of canopy growth and phenological stage progression within IXIM is GDD, and phenological

progress of corn is split into six stages: emerged, late juvenile, tasseling, silking, grainfill, mature, with an additional delay in late juvenile to tasseling progression related to cultivar day length sensitivity.

To generate synthetic crop progress data in Argentina, a single corn cultivar, DeKalb DK 752, was used in all IXIM simulations. At the time of the study, this cultivar accounted for 80% of corn seed sold within Argentina (Andrés Ferreyra et al., 2001). While it would have been possible to calibrate IXIM on BdC survey data for each district, a cultivar based upon the literature was used to preserve the ‘unsurveyed’ nature of this study. Parameters for this cultivar were taken from a field study conducted in Argentina by Andrés Ferreyra et al. (2001).

An early and a late planting corn simulation was run for each 10 km grid with a district which has historically contained corn. Early and late planted simulations were then weighted by the four-year average of the distribution of early and late planting corn in each zone to preserve the proportion of early and late planted corn present in the zone-level aggregated data (Table 1).

The historical planting window for each zone was defined as the time between the earliest and latest reported planting dates for each zone in BdC corn crop progress reports. A simple, weather-dependent planting decision model was developed to generate planting dates for each 10 km grid square to avoid fixed planting distributions, which would be learnable. DSSAT simulations were conducted in baresoil mode using the synthetic weather data, and days with average soil temperature to 30 cm depth of  $\geq 7^{\circ}\text{C}$  and moisture between 40% and 90% of the soil’s drained upper limit and permanent wilting point were considered suitable planting days. A planting date was sampled uniformly from the first ten candidate planting days after the earliest historical planting date within a zone. This random component staggered planting in adjacent grid squares and ensured synthetic planting windows were not unrealistically shortened.

Harvest dates for corn simulations were modeled as a function of simulated crop matu-

rity date and a random additional  $X$  days, where  $X \sim \mathcal{N}(30, 10)$ , to simulate the in-field dry down period between physical maturity and harvest in corn. In-field dry down, which producers use to reduce grain moisture and avoid post-harvest drying costs, is affected by weather. Dry down is not simulated within IXIM and this normal distribution was derived from the historical distribution of median maturity to harvest dates in US Midwest CPRs. Though conditions in the US Midwest differ from those in Argentina, the main objective of incorporating this random component was to avoid fixed harvest distributions.

Simulated growth stage progression for each grid was aggregated to zone level to form a CPR-style progress percentage for each stage, as defined in Table 4. IXIM-defined growth stages ‘early/late juvenile’ and ‘tasseling’ were grouped as ‘emerged’. The ‘dough’ stage, which is not explicitly demarcated with IXIM, was set as the point at which modeled grain weight reached 33% of its final weight (R.L. Nielsen, 2021). Daily LAI and soil moisture values generated by IXIM were used to parameterize SPART canopy reflectance simulations, as shown in Figure 6.

### 3.2.3. SPART

The SPART model combines four constituent RTMs together to simulate top-of-atmosphere optical reflectances from soil, leaf-canopy, and atmosphere. The atmospheric component was not used in this study because MODIS NDVI products were atmospherically corrected. Inputs to the SPART model include soil and vegetation parameters, shown in Table 3. The soil RTM within SPART is the Brightness-Shape-Moisture model, which describes all soil spectral reflectances as a combination of three ‘global soil vectors’ derived from Jiang and Fang (2019). Wet soil reflectance is modeled as a combination of a thin water film on top of a dry soil to account for the wetness component. In this study, the global soil vectors approach was replaced with dry soil reflectance data from the ECOSTRESS soil reflectance library (see Section 2.1.3) assigned to each soil grid (Meerdink et al., 2019).

The leaf-canopy component of SPART is the widely used PROSAIL coupling of the PROSPECT leaf and SAILH canopy RTMs (Jacquemoud et al., 2009). PROSPECT uses

leaf water content, chlorophyll and pigment concentration, dry matter, and internal structure information to simulation leaf reflectance and transmittance across the 400 nm to 2500 nm spectrum at 1 nm resolution. In this study, the default PROSPECT parameters were used for all SPART simulations, shown in Table 3. With LAI, leaf angle distributions, and canopy height information, SPART uses the SAILH model to translate simulated leaf reflectance to top-of-canopy canopy reflectance data by modeling light-canopy-soil interactions. Information on leaf angle distributions and canopy height by plant age, not simulated by IXIM, were obtained from corn field experiments conducted in the US (Judge et al., 2021).

Daily SPART simulations were conducted for each 10 km grid for every day from IXIM simulation start (pre-planting) until harvest. Simulated canopy reflectances at 620–670 nm ( $\rho_{Red}$ ) and 841–876 nm ( $\rho_{NIR}$ ) matching those of MODIS bands were used to produce synthetic NDVI using:

$$NDVI = \frac{\rho_{NIR} - \rho_{Red}}{\rho_{NIR} + \rho_{Red}} \quad (3)$$

Post-harvest NDVI values for each pixel were generated by sampling from the pre-planting NDVI values for that season, which had a soil moisture-dependent range of  $< 0.03$ . Synthetic NDVI data were then aggregated to zone level following the method outlined in Section 2.1.2.

SPART simulations were the most computationally demanding part of the synthetic data generation process. Because of the large number of numerical integration operations within the PROSPECT submodule, canopy reflectance simulations took an average time of 195.1 m-sec. Reusing the default leaf reflectance spectra reduced this to 1.1 m-sec, lowering the computational time required to simulate the  $\approx 400M$  NDVI pixels across all zones and seasons from 840 CPU-days to 5 CPU-days.

Thus 99 seasons of synthetic GDD, crop progress, and NDVI were produced for the 11 corn growing zones in Argentina. Figures 7 and 8 show example synthetic GDD, crop progress, and NDVI generated by the linked SWG-IXIM-SPART models for a single pixel and across a zone, respectively.

### 3.3. Network Training

#### 3.3.1. Training Sets

We investigated the effect of exposure to surveyed and synthetic crop progress data on NN performance in Argentina by implementing four different training data combinations. The first training dataset,  $U_{sur}$ , contained data from the US surveyed regions of Iowa and Illinois, over the years 2003-2020 and 2003-2017, respectively. This dataset consisted of 315 district-season combinations of crop progress data and associated NDVI and GDD histograms. This provided a measure for the NN’s transferability to an unsurveyed region. The second set,  $A_{syn}$ , contained synthetic crop progress data produced for the 11 corn-growing zones in Argentina. This dataset contained 1188 zone-season combinations of synthetic crop progress data and associated synthetic NDVI and GDD histograms.

The third set,  $A_{syn}U_{sur}$ , combined the surveyed region data with synthetic data generated for a single, target zone in Argentina. This dataset produced 11 separate training data combinations, each of which contained the surveyed region data and synthetic data generated for one of the 11 Argentine zones. The fourth set was the union of the surveyed region data from the US and synthetic data for all 11 zones in Argentina,  $A_{syn}U_{sur}$ .

In the first three datasets, all data were combined and training batches were sampled randomly across all available data.

When training on the fourth dataset,  $A_{syn}U_{sur}$ , each batch of synthetic data sampled from  $A_{syn}$  during training was paired with a batch of Midwest data sampled with replacement from the  $U_{sur}$  data. The network loss on each of these batches was averaged such that the loss back-propagated through the network for that batch was  $loss = \frac{loss_{U_{sur}} + loss_{A_{syn}}}{2}$ . This prevented overexposure to synthetic data (80% of the  $A_{syn}U_{sur}$  set) during training, which would have encouraged the network to optimize for the underlying IXIM model.

To provide a surveyed region reference (SRR), the network was also trained on the  $U_{sur}$  dataset with the 2018–2020 seasons, which contain only Iowa data, excluded. The SRR was then tested on Iowa districts for these seasons to provide a surveyed region performance



reference.

### 3.3.2. Training Methodology

During training, the Adam optimizer was used with a learning rate of  $1e^{-3}$ , an L2-regularizing weight decay factor of  $1e^{-3}$ , and a batch size of 256 (Kingma and Ba, 2017). For this study, all hyperparameters were kept the same across all training sets. When training the network, the best set of weights produced over 100 epochs were selected. Because no unsurveyed region validation data would be available during training, weight selection criteria must be based on performance on surveyed and synthetic validation data. For the datasets which contained only one type of data,  $U_{sur}$  and  $A_{syn}$ , the training data was split into 80/20 training and validation subsets, separated by growing season. The weights produced by the epoch with the lowest validation loss were selected as the final network weights for each set.

For the training sets which contained a mix of surveyed and synthetic data,  $A_{syn1}U_{sur}$  and  $A_{syn}U_{sur}$ , we used the same training/validation split as above. For these sets, we selected the weights produced by the epoch with the lowest weighted divergence in validation loss across both the  $U_{sur}$  and  $A_{syn}/A_{syn1}$  validation subsets, with weighted divergence as:

$$D = |VL_{U_{sur}} - VL_A| \times (VL_{U_{sur}} + VL_A)/2 \quad (4)$$

where  $VL_{U_{sur}}$  is the loss for the  $U_{sur}$  validation subset and  $VL_A$  is the validation loss for the  $A_{syn}$  or  $A_{syn1}$  validation subsets during training.

Figure 9 shows the location of the lowest weighted divergence for the  $A_{syn}U_{sur}$  training loss curve, with the lowest surveyed and synthetic validation loss values over 100 epochs also labeled. This selection strategy was implemented as a trade-off between performance on surveyed and synthetic Argentina data. It was based upon the hypothesis that at some point during training (around batch 3500 in Figure 9), the NN will reach a performance plateau that is achievable from learning generalizable relationships between NDVI, GDD, and crop progress which are valid for both the surveyed and synthetic data. After this point, it will begin to abandon crop progress notions in favor of optimizing for the underlying logic within

the crop model used to generate synthetic data, in order to continue to reduce the loss on the combined training set. As the network begins to overfit to IXIM, which is deterministic for set parameters, the surveyed data validation loss will start to increase. This occurs around batch 4000 in Figure 9, after which the  $U_{sur}$  and  $A_{syn}$  validation losses begin to diverge. The  $A_{syn}$  validation loss continues to reduce in tandem with the training losses for both sets, while the  $U_{sur}$  validation loss increases. In the absence of a true validation data from the unsurveyed region, we used the above weighted measure as a stopping criterion to identify the training epoch when this divergence between  $U_{sur}$  and  $A_{syn}$  validation loss began.

### 3.4. Performance Metrics

Many existing studies in crop progress target median transition date into a given stage, and use RMSE of estimated versus observed median transition date as a performance metric, e.g. Diao (2020); Gao et al. (2020a). However, from a risk perspective, knowing the proportion of a region’s crop in a given stage of crop progress at any time during the season is more descriptive. In this study, we adapt  $F_1$  score, common in ML classification studies, to evaluate CPE method accuracy, penalizing both over and underestimates of crop progress for each stage for every week within a growing season. The adapted  $F_1$  score in this study is defined as:

$$F_1 = \frac{TP}{TP + \frac{1}{2}(FP + FN)} \quad (5)$$

where TP, FP, and FN are true positive, false positive, and false negative rates, respectively, which are defined in terms of the overlap, overestimate, and underestimate of the NN-derived crop progress and the observed *in situ* values, such that:

$$\begin{aligned} TP &= \sum^W \min\{CP_w^{est}, CP_w^{obs}\} \\ FP &= \sum^W \max\{CP_w^{est} - CP_w^{obs}, 0\} \\ FN &= \sum^W \max\{CP_w^{obs} - CP_w^{est}, 0\} \end{aligned} \quad (6)$$

Where  $CP_w^{est}$  is the crop progress estimate for a stage on week  $w$  and  $CP_w^{obs}$  is the observed crop progress from ground surveys.  $F_1$  values can range from 0 to 1. An  $F_1$  score of 1 indicates the network perfectly estimated the percentage of a district/zone’s crop in that stage for every week in the season, while an  $F_1$  score of 0 means there was no overlap at all between the network estimates of crop progress timing and *in situ* crop progress through that stage. We measured overall performance through net  $F_1$  score, calculated by summing TP, FP, and FN across stages and/or zones before computing Equation 5.

After being trained on each of the four training datasets, the NN was assessed on real Argentina crop progress data from the 2019/20 and 2020/21 growing seasons, which remained unseen by the network prior to method evaluation. The performance of the network when trained on these sets was compared with its performance when trained on the SRR and evaluated on Iowa districts during the 2018–2020 seasons.

## 4. Results and Discussion

### 4.1. Overall Performance

Table 5 shows the net  $F_1$  scores from both seasons and all zones for each training set and the reference set, SRR. Even though network performance in Argentina was lower for all training sets than performance in Iowa using the SRR, the  $F_1$  scores of 0.618–0.736 are significant considering the network did not encounter any real examples of crop progress in Argentina during training. The  $A_{syn}U_{sur}$  set produced the best net  $F_1$  scores for the Pre-emergence, Emerged, Silking, and Mature stages, but, interestingly, the  $A_{syn1}U_{sur}$  set, which contains synthetic data only from the target zone, produced better scores for the Dough and Harvested stages (see Table 5). Synthetic data generation for both of these stages relies on study-defined assumptions, which may explain why including only a single zone of synthetic data produced better results for these stages. For example, the assumptions for the Dough stage include its onset at 33% grain weight and near-linear grainfill rate in unstressed conditions (Lizaso et al., 2011), as shown in Figure 7. For the Harvested stage, time between maturity and harvest is assumed to be normally distributed and independent of weather (see

Section 3.2.2). It is possible that exposure to many examples of these assumptions negatively affected performance on these stages, but the limited examples in the  $A_{syn1}U_{sur}$  set provided enough zone-specific crop progress information without overwhelming the weather-dependent relationships for these stages present in the surveyed region data. The additional synthetic data in the  $A_{syn}U_{sur}$  set, which is weighted equally with surveyed region data during training, may encourage the network to adopt these synthetic data assumptions, thereby reducing performance.

When trained on the  $U_{sur}$  set, the net  $F_1$  score was 8% lower than when trained on the best overall performing set, as shown in Table 5. Performance for  $U_{sur}$  set was lower for all stages except the Dough stage, which was marginally higher. The largest performance gap for the network when trained on the  $U_{sur}$  set was for the Mature stage, which was 19.5% lower than the  $A_{syn}U_{sur}$  set. The network also scored lower for the Mature stage when trained on the  $U_{sur}$  set than when trained on the  $A_{syn}$  set, which is interesting because this set does not contain any real crop progress data. This is possibly because the GDD to maturity of the synthetic Argentina cultivar is closer to current *in situ* Argentina cultivars than what is grown in the US Midwest. This result shows the limitations in transferability of a network to unsurveyed region CPE when trained only on data from a surveyed region with different crop growth dynamics.

#### 4.2. Impact of Including Synthetic Data

The major contribution of synthetic data is to provide examples of the expected cropping regimes from the target, unsurveyed region. In this study, the synthetic data provided examples of crop progress as produced by a dual planting cropping system. Including synthetic data during training, i.e.  $A_{syn}$ ,  $A_{syn1}U_{sur}$ , or  $A_{syn}U_{sur}$ , increased  $F_1$  scores for 57 out of 66 zone–stage combinations, and net  $F_1$  scores across all stages increased in 9 out of 11 zones for both the 2019/20 and 2020/21 test seasons, shown in Tables 6 and 7, respectively. Figures 10a–10f show the  $F_1$  scores by stages for each zone as a function of early and late planting percentage in those zones.

#### 4.2.1. Single Planting

The impact of synthetic data in single planting zones was mixed. For zones with  $\geq 85\%$  of the corn crop planted in a single window, such as VI and VII, performance when trained on  $U_{sur}$  data was similar to or better (e.g. Dough, see Figure 10d and Tables 6 and 7) than performance when trained on the  $A_{syn}U_{sur}$  and  $A_{syn1}U_{sur}$  sets. This suggests that in single planting zones, imperfect synthetic data assumptions may sometimes outweigh the limited additional context gained beyond the examples present in the  $U_{sur}$  set.

In Zone I, a 100% single planting zone, the synthetic data improved network performance. Figures 11a–11f show the NDVI and GDD histograms, synthetic and *in situ* crop progress data, and network crop progress estimates for Zone I during the 2019/20 test season, respectively. When trained on the  $A_{syn}U_{sur}$  set, the network scored higher in Zone I than any other zone across all methods in both test seasons (see Tables 6 and 7). The net  $F_1$  score across all stages for this zone during 2019/20 was 0.845 when the network was trained on the  $A_{syn}U_{sur}$  set, only 5.1% lower than the net performance in Iowa for the SRR (Table 5). For Silking, the most critical stage for corn in terms of yield loss, the  $F_1$  score was only 0.7% lower than the SRR net  $F_1$  score for both the 2019/20 and 2020/21 test seasons. When trained on the  $U_{sur}$  set, the network scored 9.6% and 6.5% lower than the  $A_{syn}U_{sur}$  set on this zone, though performance on the Dough stage was the highest using  $U_{sur}$  for both seasons (Tables 6 and 7). The network also scored highest on the Mature and Harvested stages when trained only on the  $A_{syn}$  set (see Table 6). These high scores were due to a lower false negative rate on the Mature stage and a lower false positive rate on the Harvested stage, shown in Figure 11d.

However, in Zone II, also a 100% late planting zone, performance improvement from the addition of synthetic data was mixed for the two test seasons. During the 2019/20 season, net performance was highest using the  $U_{sur}$  set at 0.723, marginally higher than the  $A_{syn1}U_{sur}$  set. The addition of synthetic data from all zones, however, reduced performance during this season, particularly for the Silking stage, which was lower for both the  $A_{syn}$  and  $A_{syn}U_{sur}$

sets (Table 6). During the 2020/21 season, net performance increased with the addition of synthetic data from all zones, but  $F_1$  scores for the Silking and Dough stages were still higher when the network was trained on the  $U_{sur}$  and  $A_{syn1}U_{sur}$  sets.

The mixed impact of including all synthetic data in these single planting zones is possibly due to the presence of dual planting examples in the  $A_{syn}$  and  $A_{syn}U_{sur}$  sets. When tasked with estimating unsurveyed region CPE in a single planting region, these dual planting examples have significantly less benefit and may cause the network to mistake any mid-season NDVI noise as the emergence of a second crop. Additional investigation would be needed to assess these effects, including increasing the proportion of single planting synthetic examples when targeting a single planting zone.

#### 4.2.2. Dual Planting

In zones where the corn crop was evenly split between early and late planting, such as Zones IX, X, and XII, hereafter mixed zones,  $F_1$  scores for  $U_{sur}$  set network were significantly lower and the positive impact of including synthetic data was more evident, as shown in Tables 6 and 7. For example, the performance gap between primarily single planting zones and mixed planting zones was significantly reduced when the network was trained on the  $A_{syn1}U_{sur}$  set, particularly for the Silking (Figure 10c) and Mature (Figure 10e) stages. This led to an overall 7.1% performance increase when compared to the  $U_{sur}$  set (see Table 5). Including synthetic data from all zones during training improved network performance further, with the largest gain for the Pre-emergence, Emerged, and Silking stages, shown in Figures 10a, 10b, and 10c.

The benefits of exposure to synthetic examples of dual planting crop progress can be seen in Zone IX, a dual planting zone in which corn progresses bi-modally through the season. Figures 12a–12f show the NDVI and GDD histograms, synthetic and *in situ* crop progress data, and network crop progress estimates for Zone IX during the 2019/20 test season, respectively. When trained on the  $U_{sur}$  data, the network produced uni-modal estimates of crop progress, shown in Figure 12c. Without exposure to synthetic examples of dual planting

crop progress during training, the network only identified the first green-up curve present in the NDVI histogram, shown in Figure 12a, and estimated near 100% emergence around DOY 300. This error continued through the season, with crop progress estimates following the early planting crop but missing the late planting crop. This caused high false positive and false negative rates on both the Silking and Dough stages. In contrast, when exposed to synthetic data in the  $A_{syn}$  (Figure 12d),  $A_{syn1}U_{sur}$  (Figure 12e), and  $A_{syn}U_{sur}$  (Figure 12f) sets during training, the network could identify and estimate the bi-modal crop progress in this zone, with higher true positive rates for stages Emerged through Mature and a lower false negative rate on the Harvested stage, as reflected in the  $F_1$  scores in Table 6. Agreement between the range of crop progress within the synthetic data for Zone IX and *in situ* crop progress for the two test seasons was high, as shown in Figure 12b, leading to high  $F_1$  scores for this zone when the network was trained on the  $A_{syn}$  and  $A_{syn1}U_{sur}$  datasets.

While the addition of synthetic data improved overall  $F_1$  scores in mixed planting zones, performance was significantly reduced when the network was exposed to synthetic data that were poorly aligned with *in situ* progress. For example, in Zone III during the 2020/21 season, shown in Figure 13, *in situ* crop progress was slower than crop progress in the synthetic data, implying the required GDD to maturity for cultivars grown in Zone III was higher than for the cultivar used in IXIM simulations. When the network was trained on the  $U_{sur}$  and  $A_{syn1}U_{sur}$  sets, network estimates had minimal overlap with *in situ* crop progress for the Silking stage, as shown in Figures 13c and 13e, respectively. This poor alignment with *in situ* Silking resulted in lower  $F_1$  scores for the Silking stage when trained on the  $A_{syn1}U_{sur}$  set than when trained on the  $U_{sur}$  set alone (see Table 7). Training on the  $A_{syn}$  and  $A_{syn}U_{sur}$  datasets, however, which contain a broader range of synthetic crop progress examples, mitigated this issue, reducing the network’s early false positive rate, shown in Figures 13d and 13f. This result suggests that using a variety of synthetic crop progress examples from multiple regions during training is preferable when cultivar information from the target region is not known *a priori*.

Combining real and synthetic data, i.e.  $A_{syn1}U_{sur}$ ,  $A_{syn}U_{sur}$ , increased network performance in most dual planting zones, but  $F_1$  scores remained very low for Zone V, shown in Figure 14, where the early and late planting windows are the most separated (see Figure 2). Network performance was low for Zone V because alignment between the range of synthetic crop progress data and *in situ* crop progress, shown in Figure 14b, was particularly poor for this zone. While this issue was mitigated when training on the  $A_{syn}$  and  $A_{syn}U_{sur}$  datasets for other zones, Zone V planting windows are so separate that synthetic data from other zones was not sufficient to provide examples which encompass *in situ* crop progress for this zone.

Another factor contributing to low performance could be the significant pre-planting and post-harvest noise in the NDVI data from off-season crops, shown in Figure 14a. Noise in the NDVI histogram caused crop progress estimates to revert from Harvested to earlier stages as the late planting NDVI curve peaked between DOY 60 and 90 (Figure 14c) and during post-season NDVI noise after DOY 210 (Figure 14f).

#### 4.3. Mitigation of NDVI Noise Sensitivity

Network sensitivity to noise in the NDVI histogram was much greater when the network was trained only on the synthetic data,  $A_{syn}$ , with no examples from a surveyed region. For example in Zone VI during the 2019/20 season, shown in Figure 15, which had 92% early planting, a late increase in NDVI from DOY 60 to 90 (Figure 15a) caused a delayed estimate of the transition from Mature to Harvested and a small reversion from Mature to Dough when the network was trained on the  $A_{syn}$  set, shown in Figure 15d. As this NDVI increase subsided, further NDVI noise between DOY 180 and 240, likely from cover crop or winter crop emergence in some fields, caused another reversion from Harvested to Mature. This sensitivity to NDVI can be explained by inspection of example NDVI histograms from the synthetic data, shown in Figure 16, which contain none of the early and late season noise caused by cover crop, double cropping, or cloud cover that is present in real NDVI data.

When trained on datasets that included surveyed region data, the network was less sensi-



tive to NDVI noise, seen in Figures 15c, 15e, and 15f. Only a small reversion occurred when the network was trained on the  $A_{syn}U_{sur}$  set, and the network was completely insensitive to this post-season noise when trained on the  $A_{syn}U_{sur}$  and  $U_{sur}$  sets. This is notable because winter cover crops and dual cropping systems are uncommon in Iowa and Illinois, suggesting the de-sensitizing component in the surveyed region data is likely observational NDVI noise, such as cloud contamination, rather than pre- and post-season cropping. This suggests that surveyed region data contributes both real crop progress examples and realistic noise profiles which improve network performance.

#### 4.4. Potential Improvements

Based upon the results of this study, we provide insights into three potential improvements to RS-based unsurveyed region CPE.

In-season CPE could be significantly improved by increasing the variety and quantity of synthetic crop progress data. In this study, we used a single cultivar in Argentina, and planting windows from the historical distribution of early and late planting for each zone. Both cultivar and planting distributions could be varied. For example, seasonal GDD ranges for each zone could be calculated, and existing viable cultivars from the IXIM library could be used to increase the variety of GDD-specific silking and maturity times within the synthetic dataset. Additionally, simulations from another crop model, such as APSIM Maize (Holzworth et al., 2014), could provide more synthetic crop progress data using different crop modeling logic. This data could be combined during training, with validation losses monitored separately to ensure that a network learns crop progress notions which are applicable to both models and as well as surveyed region data.

Secondly, the processing of RS data captured for real crop progress seasons in unsurveyed regions could be improved. The results from this study show that NDVI noise from pre- and post-season vegetation can affect network performance. This noise could be reduced by pixel-level masking of pre- and post-season NDVI signals. In this study, we used linearly interpolated pixel-level NDVI values, but higher complexity filters such as the Savitsky-Golay

method (Chen et al., 2004) could be used to smooth NDVI pixel values before aggregation. Existing trend-based techniques such as those proposed by Gao et al. (2020a,b) could then be used to estimate SOS and EOS dates on pixel-level NDVI curves. While these methods often have a delayed confirmatory signal, they may be sufficient to mask post-season pixel-level NDVI noise which affected network performance in this study, particularly in zones with a large separation between early and late planted crops, such as Zone V. Additionally, if early and late planting pixels can be differentiated in-season using crop mapping methods, it may also be possible to treat each planting window as a standalone season and remove the additional complexity required of a network to learn the dynamics of dual planting systems.

Finally, RS-based in-season CPE could be further improved using complementary information from multiple remote sensing systems. For example, this study used optical data from MODIS, but observations at other wavelengths, such as microwaves from the Sentinel 1 and upcoming NISAR missions, could provide additional guidance for canopy properties such as soil and vegetation water content and biomass. This could improve differentiation between crop progress stages, and their synthetic equivalents could be modeled using radiative transfer models linked to the synthetic data generation process.

## 5. Conclusions

Existing crop progress estimation methods have been limited to surveyed regions due to the requirement of *in situ*, ground survey data for method training/calibration. In this study, we linked existing weather, crop, and optical RTM models to produce synthetic examples of crop progress for an unsurveyed region. Using Argentina as a test ‘unsurveyed’ region surrogate, we combined surveyed crop progress data from the US Midwest and synthetic data produced for zones in Argentina to train an LSTM-based NN for in-season CPE. Adapting  $F_1$  score to measure CPE accuracy, results showed that introducing synthetic data into the training set improved network CPE performance, particularly in regions with two separate planting windows. Net  $F_1$  scores across all six target stages of corn crop progress in Argentina increased by 8.7% when exposed to a combination of surveyed region and synthetic

data during training, with performance most improved in dual planting zones. Results also showed that surveyed region data helps mitigate network sensitivity to NDVI noise. Overall, unsurveyed region performance was only 21% lower than the best case scenario, when the same network was trained and evaluated in surveyed US Midwest states. This result is significant given that the network had never seen real crop progress examples from Argentina during training.

Building upon the results of this study, we outlined areas that could further improve the accuracy of CPE in unsurveyed regions, including seasonal masking of NDVI and increasing the quantity and variety of synthetic data. The aim of this study was in-season CPE in unsurveyed regions, but the method for generating synthetic data for network training presented here could also be applied to other areas of agricultural RS, such as crop mapping and yield estimation in both surveyed and unsurveyed regions.

### **Declaration of Interest**

The authors declare that they have no known competing financial interests or personal relationships that could have appeared to influence the work reported in this paper.

### **Acknowledgments**

We gratefully acknowledge the USDA-NASS Upper Midwest and Heartland Regional Offices for providing the tabulated data from USDA Crop Progress and Condition reports. This study was funded in part by the University of Florida Informatics Institute, the University of Florida Center for Remote Sensing, and USDA-NRCS CIG Grant AGR00020960.

### **References**

de Abelleira, D., Veron, S., Banchemo, S., Mosciaro, M., Propato, T., Ferraina, A., Taffarel, M.C.G., Dacunto, L., Franzoni, A., Volante, J., 2020. First Large Extent and High Resolution Cropland and Crop Type Map of Argentina, in: 2020 IEEE

- Latin American GRSS & ISPRS Remote Sensing Conference (LAGIRS), IEEE, Santiago, Chile. pp. 392–396. URL: <https://ieeexplore.ieee.org/document/9165610/>, doi:10.1109/LAGIRS48042.2020.9165610.
- Akhavizadegan, F., Ansarifard, J., Wang, L., Huber, I., Archontoulis, S.V., 2021. A time-dependent parameter estimation framework for crop modeling. *Scientific Reports* 11, 11437. URL: <http://www.nature.com/articles/s41598-021-90835-x>, doi:10.1038/s41598-021-90835-x.
- Andrés Ferreyra, R., Podestá, G.P., Messina, C.D., Letson, D., Dardanelli, J., Guevara, E., Meira, S., 2001. A linked-modeling framework to estimate maize production risk associated with ENSO-related climate variability in Argentina. *Agricultural and Forest Meteorology* 107, 177–192. URL: <https://linkinghub.elsevier.com/retrieve/pii/S0168192300002409>, doi:10.1016/S0168-1923(00)00240-9.
- Apipattanavis, S., Bert, F., Podestá, G., Rajagopalan, B., 2010. Linking weather generators and crop models for assessment of climate forecast outcomes. *Agricultural and Forest Meteorology* 150, 166–174. URL: <https://linkinghub.elsevier.com/retrieve/pii/S0168192309002287>, doi:10.1016/j.agrformet.2009.09.012.
- Archontoulis, S.V., Castellano, M.J., Licht, M.A., Nichols, V., Baum, M., Huber, I., Martinez-Feria, R., Puntel, L., Ordóñez, R.A., Iqbal, J., Wright, E.E., Dietzel, R.N., Helmers, M., Vanloocke, A., Liebman, M., Hatfield, J.L., Herzmann, D., Córdova, S.C., Edmonds, P., Togliatti, K., Kessler, A., Danalatos, G., Pasley, H., Pederson, C., Lamkey, K.R., 2020. Predicting crop yields and soil-plant nitrogen dynamics in the US Corn Belt. *Crop Science* 60, 721–738. URL: <https://onlinelibrary.wiley.com/doi/10.1002/csc2.20039>, doi:10.1002/csc2.20039.
- Chakrabarti, S., Bongiovanni, T., Judge, J., Nagarajan, K., Principe, J.C., 2015. Downscaling Satellite-Based Soil Moisture in Heterogeneous Regions Using High-Resolution Remote

- Sensing Products and Information Theory: A Synthetic Study. *IEEE Transactions on Geoscience and Remote Sensing* 53, 17.
- Chen, J., Jönsson, P., Tamura, M., Gu, Z., Matsushita, B., Eklundh, L., 2004. A simple method for reconstructing a high-quality NDVI time-series data set based on the Savitzky–Golay filter. *Remote Sensing of Environment* 91, 332–344. URL: <https://linkinghub.elsevier.com/retrieve/pii/S003442570400080X>, doi:10.1016/j.rse.2004.03.014.
- Cheng, G., Xie, X., Han, J., Guo, L., Xia, G.S., 2020. Remote Sensing Image Scene Classification Meets Deep Learning: Challenges, Methods, Benchmarks, and Opportunities. *IEEE Journal of Selected Topics in Applied Earth Observations and Remote Sensing* 13, 3735–3756. URL: <https://ieeexplore.ieee.org/document/9127795/>, doi:10.1109/JSTARS.2020.3005403.
- Cheng, Y., Zhu, H., Wu, J., Shao, X., 2019. Machine Health Monitoring Using Adaptive Kernel Spectral Clustering and Deep Long Short-Term Memory Recurrent Neural Networks. *IEEE Transactions on Industrial Informatics* 15, 987–997. URL: <https://ieeexplore.ieee.org/document/8444085/>, doi:10.1109/TII.2018.2866549.
- Claassen, M.M., Shaw, R.H., 1970. Water Deficit Effects on Corn. II. Grain Components. *Agronomy Journal* 62, 652–655. URL: <https://onlinelibrary.wiley.com/doi/abs/10.2134/agronj1970.00021962006200050032x>, doi:10.2134/agronj1970.00021962006200050032x.
- Colussi, J., Schnitkey, G., 2021. Safrinha Corn Projections Shrink as Prices in Brazil Hit Record High • farmdoc daily. URL: <https://farmdocdaily.illinois.edu/2021/06/safrinha-corn-projections-shrink-as-prices-in-brazil-hit-record-high.html>.

- Departamento de Estimaciones Agrícolas, 2020. Guía Metodológica de Estimaciones Agrícolas.
- Diao, C., 2020. Remote sensing phenological monitoring framework to characterize corn and soybean physiological growing stages. *Remote Sensing of Environment* 248. doi:10.1016/j.rse.2020.111960.
- Diao, C., Yang, Z., Gao, F., Zhang, X., Yang, Z., 2021. Hybrid phenology matching model for robust crop phenological retrieval. *ISPRS Journal of Photogrammetry and Remote Sensing* 181, 308–326. URL: <https://linkinghub.elsevier.com/retrieve/pii/S0924271621002434>, doi:10.1016/j.isprsjprs.2021.09.011.
- Doss, B.D., Pearson, R.W., Rogers, H.T., 1974. Effect of Soil Water Stress at Various Growth Stages on Soybean Yield. *Agronomy Journal* 66, 297–299. URL: <https://onlinelibrary.wiley.com/doi/10.2134/agronj1974.00021962006600020032x>, doi:10.2134/agronj1974.00021962006600020032x.
- Duan, S.B., Li, Z.L., Wu, H., Tang, B.H., Ma, L., Zhao, E., Li, C., 2014. Inversion of the PROSAIL model to estimate leaf area index of maize, potato, and sunflower fields from unmanned aerial vehicle hyperspectral data. *International Journal of Applied Earth Observation and Geoinformation* 26, 12–20. URL: <https://linkinghub.elsevier.com/retrieve/pii/S0303243413000561>, doi:10.1016/j.jag.2013.05.007.
- Duncan, J.M.A., Dash, J., Atkinson, P.M., 2015. The potential of satellite-observed crop phenology to enhance yield gap assessments in smallholder landscapes. *Frontiers in Environmental Science* 3. URL: <http://journal.frontiersin.org/Article/10.3389/fenvs.2015.00056/abstract>, doi:10.3389/fenvs.2015.00056.
- FAO, 2022. FAOSTAT. URL: <https://www.fao.org/faostat/en/#data/QCL>.
- Fassnacht, F.E., Latifi, H., Hartig, F., 2018. Using synthetic data to evaluate the benefits of large field plots for forest biomass estimation with LiDAR. *Remote Sensing of*

- Environment 213, 115–128. URL: <https://linkinghub.elsevier.com/retrieve/pii/S0034425718302281>, doi:10.1016/j.rse.2018.05.007.
- Gao, F., Anderson, M., Daughtry, C., Karnieli, A., Hively, D., Kustas, W., 2020a. A within-season approach for detecting early growth stages in corn and soybean using high temporal and spatial resolution imagery. *Remote Sensing of Environment* 242. doi:10.1016/j.rse.2020.111752.
- Gao, F., Anderson, M.C., Hively, W.D., 2020b. Detecting Cover Crop End-Of-Season Using VEN $\mu$ S and Sentinel-2 Satellite Imagery. *Remote Sensing* 12, 3524. URL: <https://www.mdpi.com/2072-4292/12/21/3524>, doi:10.3390/rs12213524.
- Gao, F., Zhang, X., 2021. Mapping Crop Phenology in Near Real-Time Using Satellite Remote Sensing: Challenges and Opportunities. *Journal of Remote Sensing* 2021, 1–14. URL: <https://spj.sciencemag.org/journals/remotesensing/2021/8379391/>, doi:10.34133/2021/8379391.
- Ghamghami, M., Ghahreman, N., Irannejad, P., Pezeshk, H., 2020. A parametric empirical Bayes (PEB) approach for estimating maize progress percentage at field scale. *Agricultural and Forest Meteorology* 281, 107829. URL: <https://linkinghub.elsevier.com/retrieve/pii/S0168192319304459>, doi:10.1016/j.agrformet.2019.107829.
- Han, E., Ines, A.V., Koo, J., 2019. Development of a 10-km resolution global soil profile dataset for crop modeling applications. *Environmental Modelling & Software* 119, 70–83. URL: <https://linkinghub.elsevier.com/retrieve/pii/S1364815218313033>, doi:10.1016/j.envsoft.2019.05.012.
- Han, W., Wang, L., Feng, R., Gao, L., Chen, X., Deng, Z., Chen, J., Liu, P., 2020. Sample generation based on a supervised Wasserstein Generative Adversarial Network for high-resolution remote-sensing scene classification. *Information Sciences* 539, 177–194. URL:

<https://linkinghub.elsevier.com/retrieve/pii/S002002552030606X>, doi:10.1016/j.ins.2020.06.018.

Hengl, T., Mendes de Jesus, J., Heuvelink, G.B.M., Ruiperez Gonzalez, M., Kilibarda, M., Blagotić, A., Shangguan, W., Wright, M.N., Geng, X., Bauer-Marschallinger, B., Guevara, M.A., Vargas, R., MacMillan, R.A., Batjes, N.H., Leenaars, J.G.B., Ribeiro, E., Wheeler, I., Mantel, S., Kempen, B., 2017. SoilGrids250m: Global gridded soil information based on machine learning. *PLOS ONE* 12, e0169748. URL: <https://dx.plos.org/10.1371/journal.pone.0169748>, doi:10.1371/journal.pone.0169748.

Holzworth, D.P., Huth, N.I., deVoil, P.G., Zurcher, E.J., Herrmann, N.I., McLean, G., Chenu, K., van Oosterom, E.J., Snow, V., Murphy, C., Moore, A.D., Brown, H., Whish, J.P., Verrall, S., Fainges, J., Bell, L.W., Peake, A.S., Poulton, P.L., Hochman, Z., Thorburn, P.J., Gaydon, D.S., Dalgliesh, N.P., Rodriguez, D., Cox, H., Chapman, S., Doherty, A., Teixeira, E., Sharp, J., Cichota, R., Vogeler, I., Li, F.Y., Wang, E., Hammer, G.L., Robertson, M.J., Dimes, J.P., Whitbread, A.M., Hunt, J., van Rees, H., McClelland, T., Carberry, P.S., Hargreaves, J.N., MacLeod, N., McDonald, C., Harsdorf, J., Wedgwood, S., Keating, B.A., 2014. APSIM – Evolution towards a new generation of agricultural systems simulation. *Environmental Modelling & Software* 62, 327–350. URL: <https://linkinghub.elsevier.com/retrieve/pii/S1364815214002102>, doi:10.1016/j.envsoft.2014.07.009.

Jacquemoud, S., Verhoef, W., Baret, F., Bacour, C., Zarco-Tejada, P.J., Asner, G.P., François, C., Ustin, S.L., 2009. PROSPECT+SAIL models: A review of use for vegetation characterization. *Remote Sensing of Environment* 113, S56–S66. URL: <https://linkinghub.elsevier.com/retrieve/pii/S0034425709000765>, doi:10.1016/j.rse.2008.01.026.

Jay, S., Maupas, F., Bendoula, R., Gorretta, N., 2017. Retrieving LAI, chlorophyll and nitrogen contents in sugar beet crops from multi-angular optical remote sensing:



- Comparison of vegetation indices and PROSAIL inversion for field phenotyping. *Field Crops Research* 210, 33–46. URL: <https://linkinghub.elsevier.com/retrieve/pii/S0378429017300175>, doi:10.1016/j.fcr.2017.05.005.
- Jenkerson, C., Maiersperger, T., Schmidt, G., 2010. eMODIS: A User-Friendly Data Source. Technical Report. US Department of the Interior, US Geological Survey. URL: <https://pubs.usgs.gov/of/2010/1055/>.
- Jiang, C., Fang, H., 2019. GSV: a general model for hyperspectral soil reflectance simulation. *International Journal of Applied Earth Observation and Geoinformation* 83, 101932. doi:10.1016/j.jag.2019.101932.
- Jones, C., Ritchie, J., Kiniry, J., Godwin, D., Otter, S., 1983. The CERES wheat and maize models, in: *Proceedings of the International Symposium on Minimum Data Sets for Agrotechnology Transfer*, ICRISAT Center, India, pp. 95–100.
- Jones, J., Hoogenboom, G., Porter, C., Boote, K., Batchelor, W., Hunt, L., Wilkens, P., Singh, U., Gijsman, A., Ritchie, J., 2003. The DSSAT cropping system model. *European Journal of Agronomy* 18, 235–265. URL: <https://linkinghub.elsevier.com/retrieve/pii/S1161030102001077>, doi:10.1016/S1161-0301(02)00107-7.
- Judge, J., Liu, P.W., Monsiváis-Huertero, A., Bongiovanni, T., Chakrabarti, S., Steele-Dunne, S.C., Preston, D., Allen, S., Bermejo, J.P., Rush, P., DeRoo, R., Colliander, A., Cosh, M., 2021. Impact of vegetation water content information on soil moisture retrievals in agricultural regions: An analysis based on the SMAPVEX16-MicroWEX dataset. *Remote Sensing of Environment* 265, 112623. URL: <https://linkinghub.elsevier.com/retrieve/pii/S0034425721003436>, doi:10.1016/j.rse.2021.112623.
- Kerner, H.R., Sahajpal, R., Pai, D.B., Skakun, S., Puricelli, E., Hosseini, M., Meyer, S., Becker-Reshef, I., 2022. Phenological normalization can improve in-season classification of maize and soybean: A case study in the central US Corn Belt. *Science*

- of Remote Sensing , 100059URL: <https://linkinghub.elsevier.com/retrieve/pii/S2666017222000219>, doi:10.1016/j.srs.2022.100059.
- Khaki, S., Pham, H., Wang, L., 2021. Simultaneous corn and soybean yield prediction from remote sensing data using deep transfer learning. *Scientific Reports* 11, 11132. URL: <http://www.nature.com/articles/s41598-021-89779-z>, doi:10.1038/s41598-021-89779-z.
- Kingma, D.P., Ba, J., 2017. Adam: A Method for Stochastic Optimization. URL: <http://arxiv.org/abs/1412.6980>.
- Koo, J., Dimes, J., 2013. HC27 Generic Soil Profile Database. URL: <https://dataverse.harvard.edu/citation?persistentId=doi:10.7910/DVN/90WJ9W>.
- Liu, L., Zhang, X., Yu, Y., Gao, F., Yang, Z., 2018. Real-Time Monitoring of Crop Phenology in the Midwestern United States Using VIIRS Observations. *Remote Sensing* 10, 1540. URL: <http://www.mdpi.com/2072-4292/10/10/1540>, doi:10.3390/rs10101540.
- Lizaso, J.I., Boote, K.J., Jones, J.W., Porter, C.H., Echarte, L., Westgate, M.E., Sonohat, G., 2011. CSM-IXIM: A New Maize Simulation Model for DSSAT Version 4.5. *Agronomy Journal* 103, 14.
- Lobell, D.B., Thau, D., Seifert, C., Engle, E., Little, B., 2015. A scalable satellite-based crop yield mapper. *Remote Sensing of Environment* 164, 324–333. URL: <https://linkinghub.elsevier.com/retrieve/pii/S0034425715001637>, doi:10.1016/j.rse.2015.04.021.
- Luo, Y., Zhang, Z., Zhang, L., Han, J., Cao, J., Zhang, J., 2022. Developing High-Resolution Crop Maps for Major Crops in the European Union Based on Transductive Transfer Learning and Limited Ground Data. *Remote Sensing* 14, 1809. URL: <https://www.mdpi.com/2072-4292/14/8/1809>, doi:10.3390/rs14081809.

- Meerdink, S.K., Hook, S.J., Roberts, D.A., Abbott, E.A., 2019. The ECOSTRESS spectral library version 1.0. *Remote Sensing of Environment* 230, 111196. URL: <https://linkinghub.elsevier.com/retrieve/pii/S0034425719302081>, doi:10.1016/j.rse.2019.05.015.
- Mehrabi, Z., Ramankutty, N., 2019. Synchronized failure of global crop production. *Nature Ecology & Evolution* 3, 780–786. URL: <http://www.nature.com/articles/s41559-019-0862-x>, doi:10.1038/s41559-019-0862-x.
- NASA Langley Research Center, . NASA POWER | Prediction Of Worldwide Energy Resources. URL: <https://power.larc.nasa.gov/>.
- Nowakowski, A., Mrziglod, J., Spiller, D., Bonifacio, R., Ferrari, I., Mathieu, P.P., Garcia-Herranz, M., Kim, D.H., 2021. Crop type mapping by using transfer learning. *International Journal of Applied Earth Observation and Geoinformation* 98, 102313. URL: <https://linkinghub.elsevier.com/retrieve/pii/S0303243421000209>, doi:10.1016/j.jag.2021.102313.
- Qian, X., Chen, X., Yue, W., Liu, X., Guo, J., Li, Z., Li, Y., Wang, W., 2020. Generating and Sifting Pseudolabeled Samples for Improving the Performance of Remote Sensing Image Scene Classification. *IEEE Journal of Selected Topics in Applied Earth Observations and Remote Sensing* 13, 4925–4933. URL: <https://ieeexplore.ieee.org/document/9178417/>, doi:10.1109/JSTARS.2020.3019582.
- Ray, D.K., Gerber, J.S., MacDonald, G.K., West, P.C., 2015. Climate variation explains a third of global crop yield variability. *Nature Communications* 6, 5989. URL: <http://www.nature.com/articles/ncomms6989>, doi:10.1038/ncomms6989.
- R.L. Nielsen, 2021. Grain Fill Stages in Corn (Purdue University). URL: <https://www.agry.purdue.edu/ext/corn/news/timeless/grainfill.html>.

- Schwalbert, R.A., Amado, T., Corassa, G., Pott, L.P., Prasad, P., Ciampitti, I.A., 2020. Satellite-based soybean yield forecast: Integrating machine learning and weather data for improving crop yield prediction in southern Brazil. *Agricultural and Forest Meteorology* 284, 107886. URL: <https://linkinghub.elsevier.com/retrieve/pii/S0168192319305027>, doi:10.1016/j.agrformet.2019.107886.
- Semenov, M.A., Barrow, E.M., 1997. Use of a stochastic weather generator in the development of climate change scenarios. *Climatic Change* 35, 397–414. URL: <http://link.springer.com/10.1023/A:1005342632279>, doi:10.1023/A:1005342632279.
- Seo, B., Lee, J., Lee, K.D., Hong, S., Kang, S., 2019. Improving remotely-sensed crop monitoring by NDVI-based crop phenology estimators for corn and soybeans in Iowa and Illinois, USA. *Field Crops Research* 238, 113–128. URL: <https://linkinghub.elsevier.com/retrieve/pii/S0378429017317379>, doi:10.1016/j.fcr.2019.03.015.
- Shen, Y., Wu, L., Di, L., Yu, G., Tang, H., Yu, G., Shao, Y., 2013. Hidden Markov Models for Real-Time Estimation of Corn Progress Stages Using MODIS and Meteorological Data. *Remote Sensing* 5, 1734–1753. URL: <http://www.mdpi.com/2072-4292/5/4/1734>, doi:10.3390/rs5041734.
- Song, X., Liu, Y., Xue, L., Wang, J., Zhang, J., Wang, J., Jiang, L., Cheng, Z., 2020. Time-series well performance prediction based on Long Short-Term Memory (LSTM) neural network model. *Journal of Petroleum Science and Engineering* 186, 106682. URL: <https://linkinghub.elsevier.com/retrieve/pii/S0920410519311039>, doi:10.1016/j.petrol.2019.106682.
- Supit, I., van Diepen, C., de Wit, A., Wolf, J., Kabat, P., Baruth, B., Ludwig, F., 2012. Assessing climate change effects on European crop yields using the Crop Growth Monitoring System and a weather generator. *Agricultural and Forest Meteorology* 164, 96–

111. URL: <https://linkinghub.elsevier.com/retrieve/pii/S0168192312001748>, doi:10.1016/j.agrformet.2012.05.005.
- USDA Ag Data Commons, 2021. CropScape - Cropland Data Layer. URL: <https://data.nal.usda.gov/dataset/cropscape-cropland-data-layer>.
- USDA National Agricultural Statistics Service, a. Charts and Maps - District and County Boundary Maps by State. URL: [https://www.nass.usda.gov/Charts\\_and\\_Maps/Crops\\_County/boundary\\_maps/indexgif.php](https://www.nass.usda.gov/Charts_and_Maps/Crops_County/boundary_maps/indexgif.php).
- USDA National Agricultural Statistics Service, b. National Crop Progress. URL: [https://www.nass.usda.gov/Publications/National\\_Crop\\_Progress/](https://www.nass.usda.gov/Publications/National_Crop_Progress/).
- Vintrou, E., Bégué, A., Baron, C., Saad, A., Lo Seen, D., Traoré, S., 2014. A Comparative Study on Satellite- and Model-Based Crop Phenology in West Africa. *Remote Sensing* 6, 1367–1389. URL: <http://www.mdpi.com/2072-4292/6/2/1367>, doi:10.3390/rs6021367.
- Wilks, D., 1998. Multisite generalization of a daily stochastic precipitation generation model. *Journal of Hydrology* 210, 178–191. URL: <https://linkinghub.elsevier.com/retrieve/pii/S0022169498001863>, doi:10.1016/S0022-1694(98)00186-3.
- Wilks, D., 1999. Simultaneous stochastic simulation of daily precipitation, temperature and solar radiation at multiple sites in complex terrain. *Agricultural and Forest Meteorology* 96, 85–101. URL: <https://linkinghub.elsevier.com/retrieve/pii/S0168192399000374>, doi:10.1016/S0168-1923(99)00037-4.
- Worrall, G., 2022. Spatial Stochastic Weather Generator. URL: <https://github.com/wirrell/SpatialWeatherGenerator>.
- Worrall, G., Rangarajan, A., Judge, J., 2021. Domain-Guided Machine Learning for Re-

- motely Sensed In-Season Crop Growth Estimation. *Remote Sensing* 13, 4605. URL: <https://www.mdpi.com/2072-4292/13/22/4605>, doi:10.3390/rs13224605.
- Worrall, G.R., Judge, J., Boote, K., Rangarajan, A., 2022. In-season crop progress estimation using remote sensing and model-guided machine learning. *agriRxiv* 2022, 20220069927. URL: <http://www.cabidigitallibrary.org/doi/10.31220/agriRxiv.2022.00131>, doi:10.31220/agriRxiv.2022.00131.
- Yang, P., van der Tol, C., Yin, T., Verhoef, W., 2020. The SPART model: A soil-plant-atmosphere radiative transfer model for satellite measurements in the solar spectrum. *Remote Sensing of Environment* 247. doi:10.1016/j.rse.2020.111870.
- Zeyer, A., Bahar, P., Irie, K., Schluter, R., Ney, H., 2019. A Comparison of Transformer and LSTM Encoder Decoder Models for ASR, in: 2019 IEEE Automatic Speech Recognition and Understanding Workshop (ASRU), IEEE, SG, Singapore. pp. 8–15. URL: <https://ieeexplore.ieee.org/document/9004025/>, doi:10.1109/ASRU46091.2019.9004025.

6. Figures

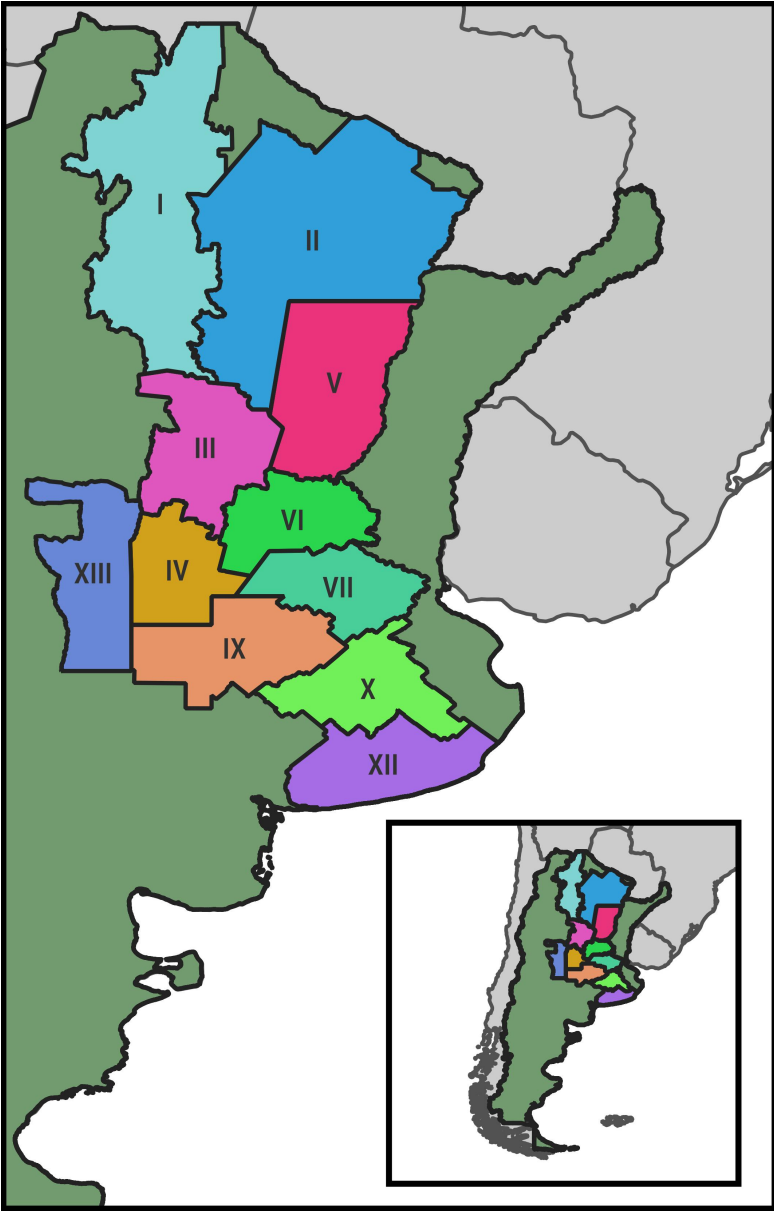


Figure 1: Bolsa de Cereales-defined corn growing zones in Argentina (Departamento de Estimaciones Agrícolas, 2020).

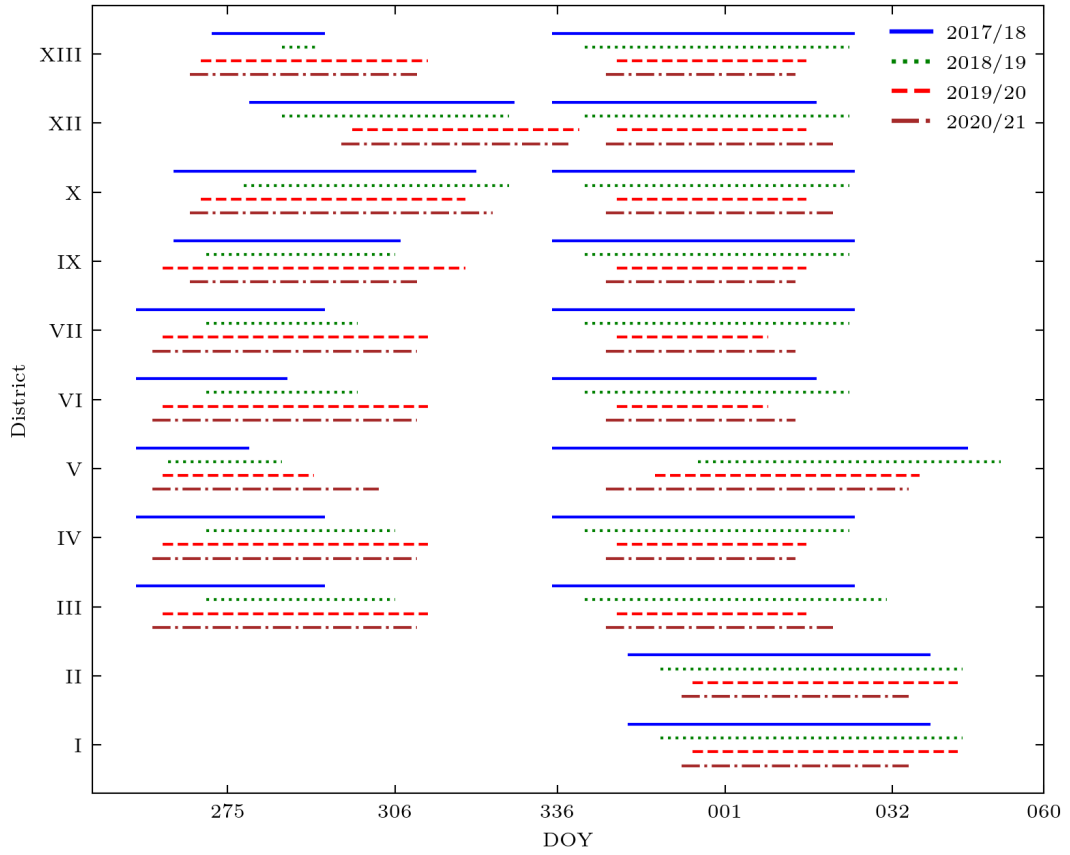


Figure 2: Early and late planting windows for corn growing zones in Argentina. Zones I and II have only one corn planting window.



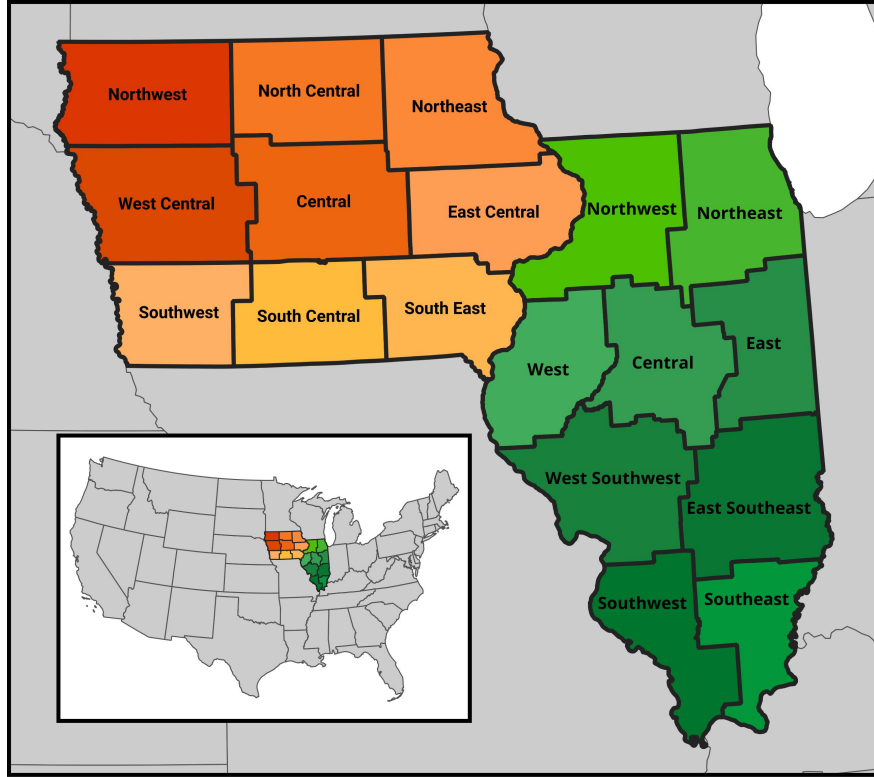


Figure 3: USDA-defined Agricultural Statistical Districts in Iowa (left) and Illinois (right) (USDA National Agricultural Statistics Service, a).

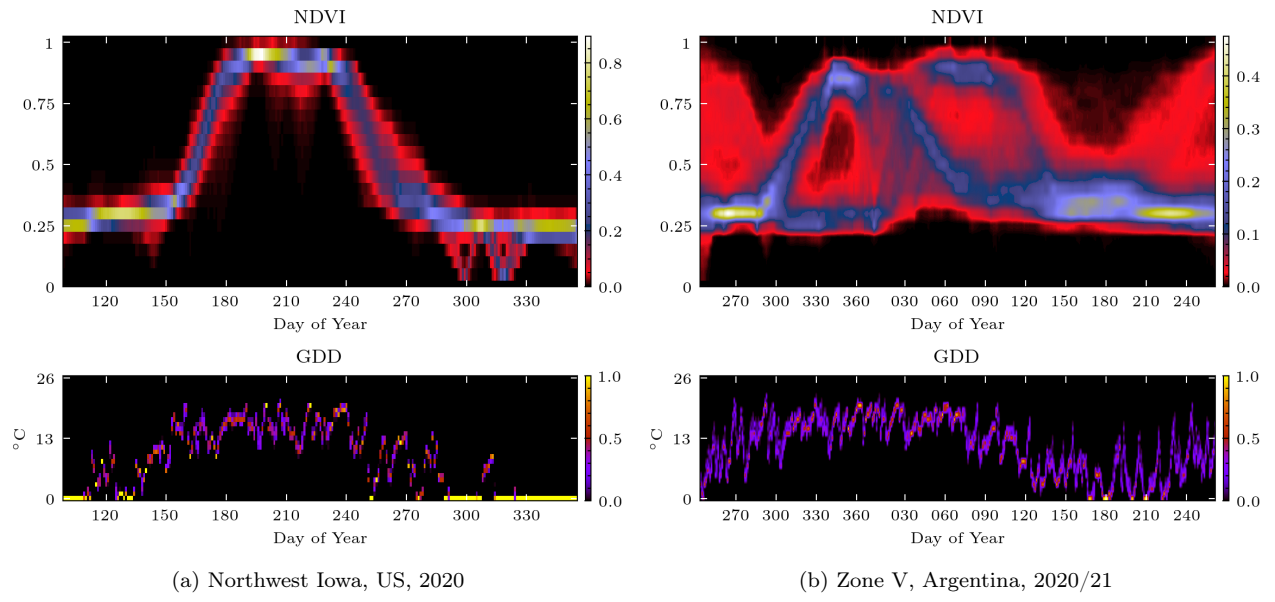


Figure 4: Example daily Normal Difference Vegetation Index (NDVI) and growing degree day (GDD) histograms inputs from (a) the US and (b) Argentina. NDVI noise related to winter-summer cropping systems and post-season cover cropping can be observed at the beginning and end of the NDVI histogram in (b).

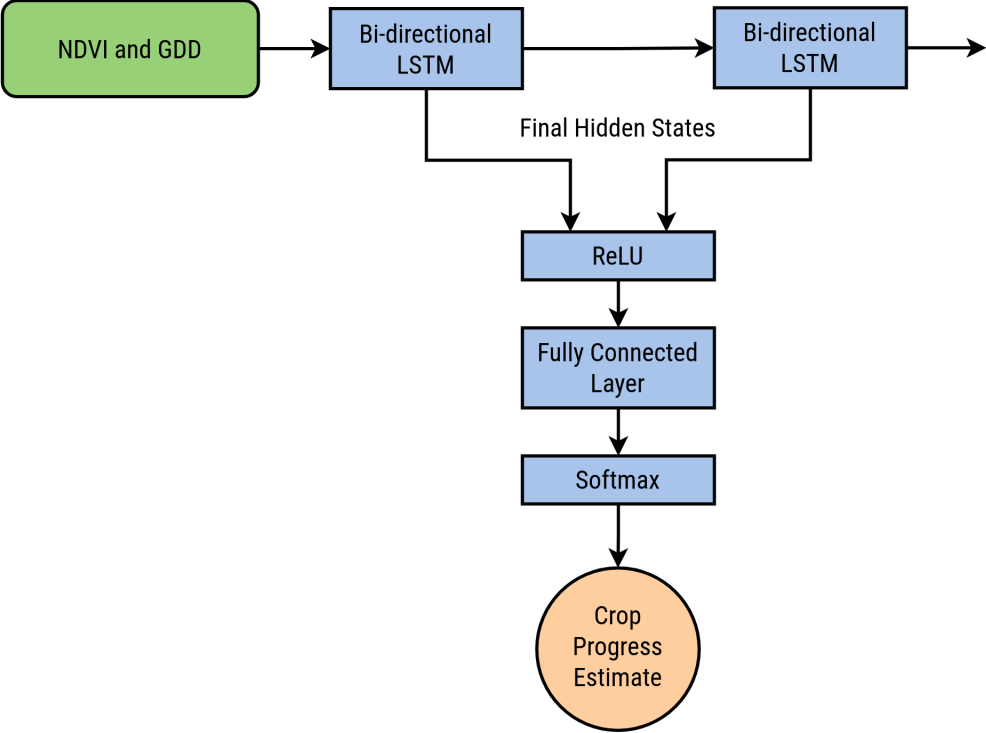


Figure 5: Structure of neural network used for in-season CPE in this study.

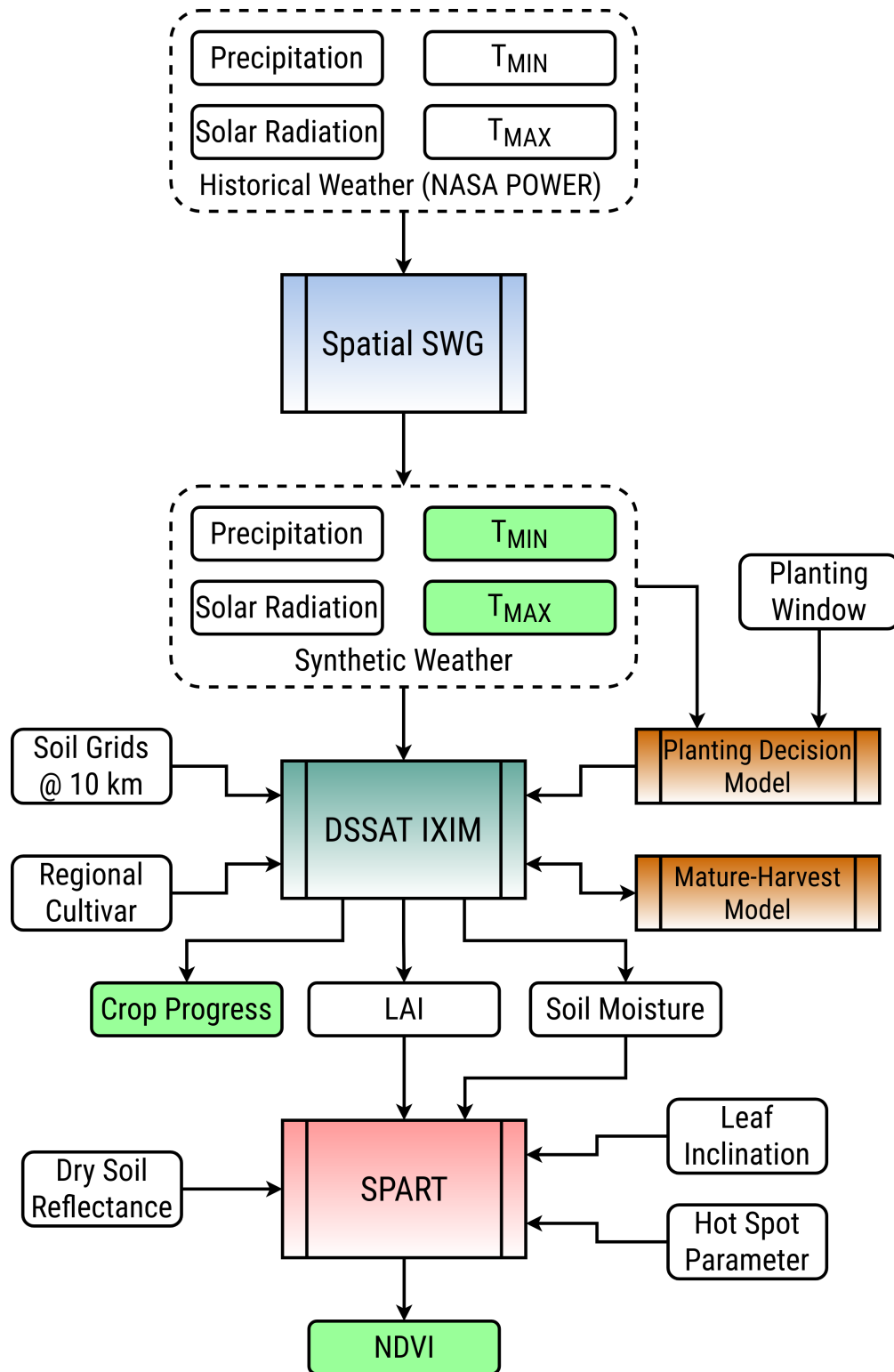


Figure 6: The linked spatial stochastic weather generator (SWG), crop model (DSSAT IXIM), and optical radiative transfer model (SPART) used for synthetic crop progress data generation in this study. The synthetic dataset includes the variables highlighted in green.

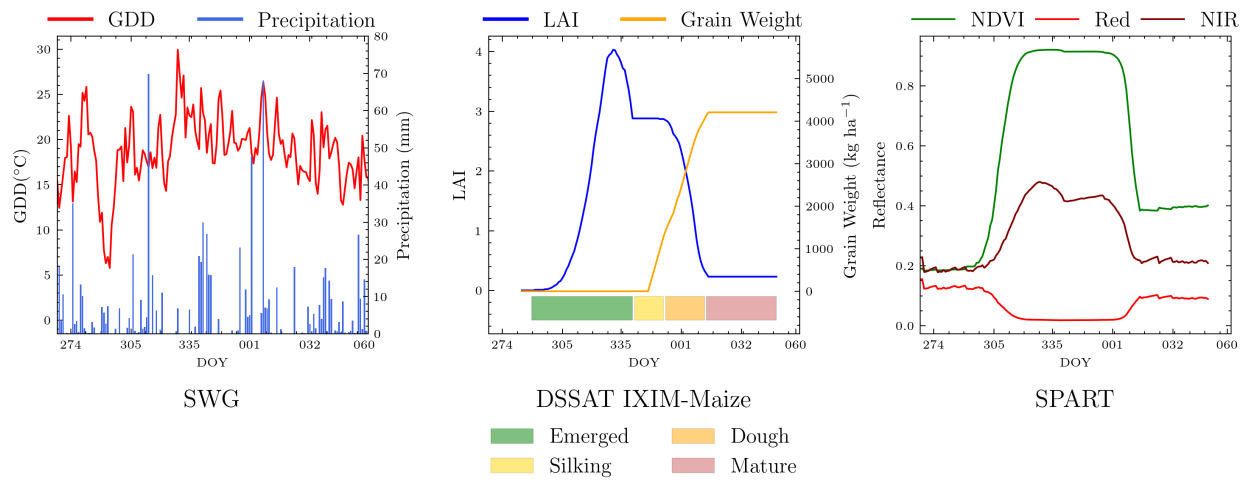


Figure 7: Example outputs produced by a linked SWG-IXIM-SPART simulation for one 10 km grid in Zone V in Argentina.

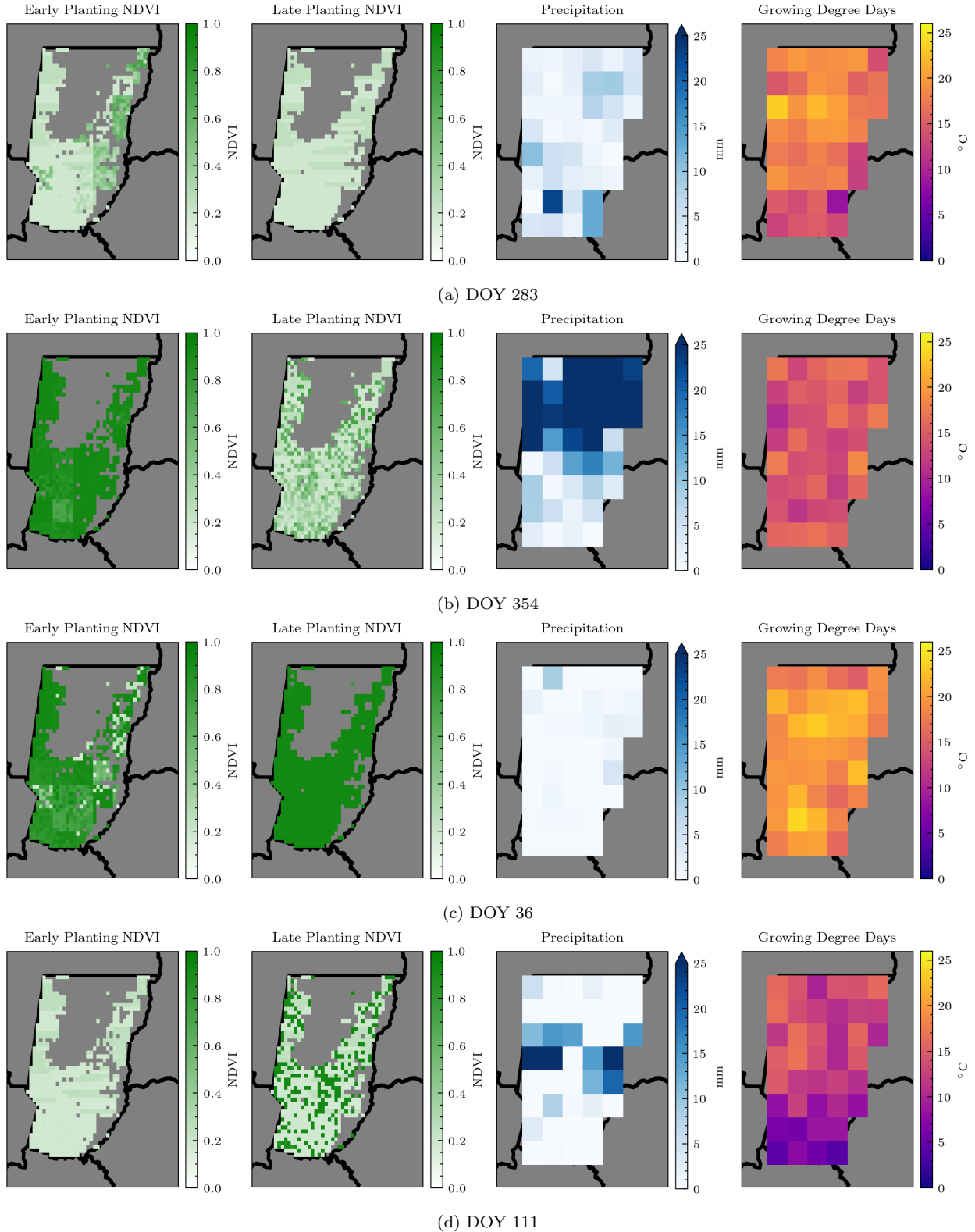


Figure 8: Examples of NDVI, precipitation, and GDD from four samples days within a full season simulation generated by the linked SWG-IXIM-SPART models in Zone V in Argentina. In (a), emergence has begun in the north eastern part of the zone, while the late planting pixels have yet to be planted. In (b), early planting pixels are at the height of their canopy growth, while emergence begins in late planting pixels across the zone. In (c), some harvest of early planting pixels has begun in the north eastern part of the zone, while late planting pixels are at the height of their growth. In (d), harvest for early planting pixels is complete, while around half of late planting pixels have been harvested. Blank areas in the NDVI plots within the zone did not contain corn in the historical crop maps from de Abelleyra et al. (2020).

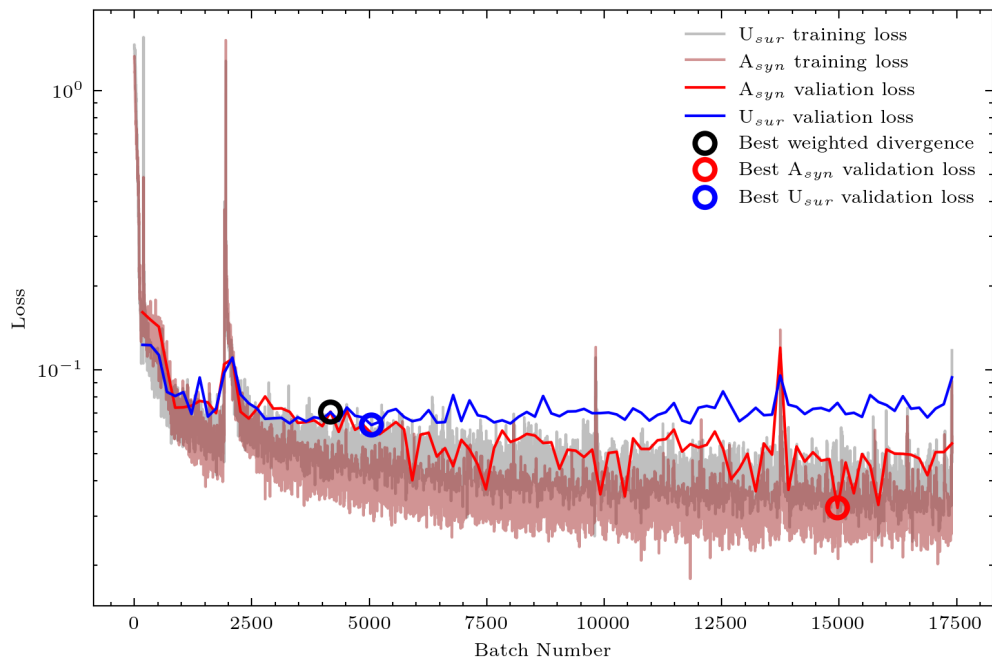


Figure 9: Training and validation loss for the NN-based in-season CPE method trained on the  $A_{syn}U_{sur}$  dataset. The three circles show the locations of the best weighted divergence measure and validation losses for the  $A_{syn}$  and  $U_{sur}$  data outlined in Section 3.3.

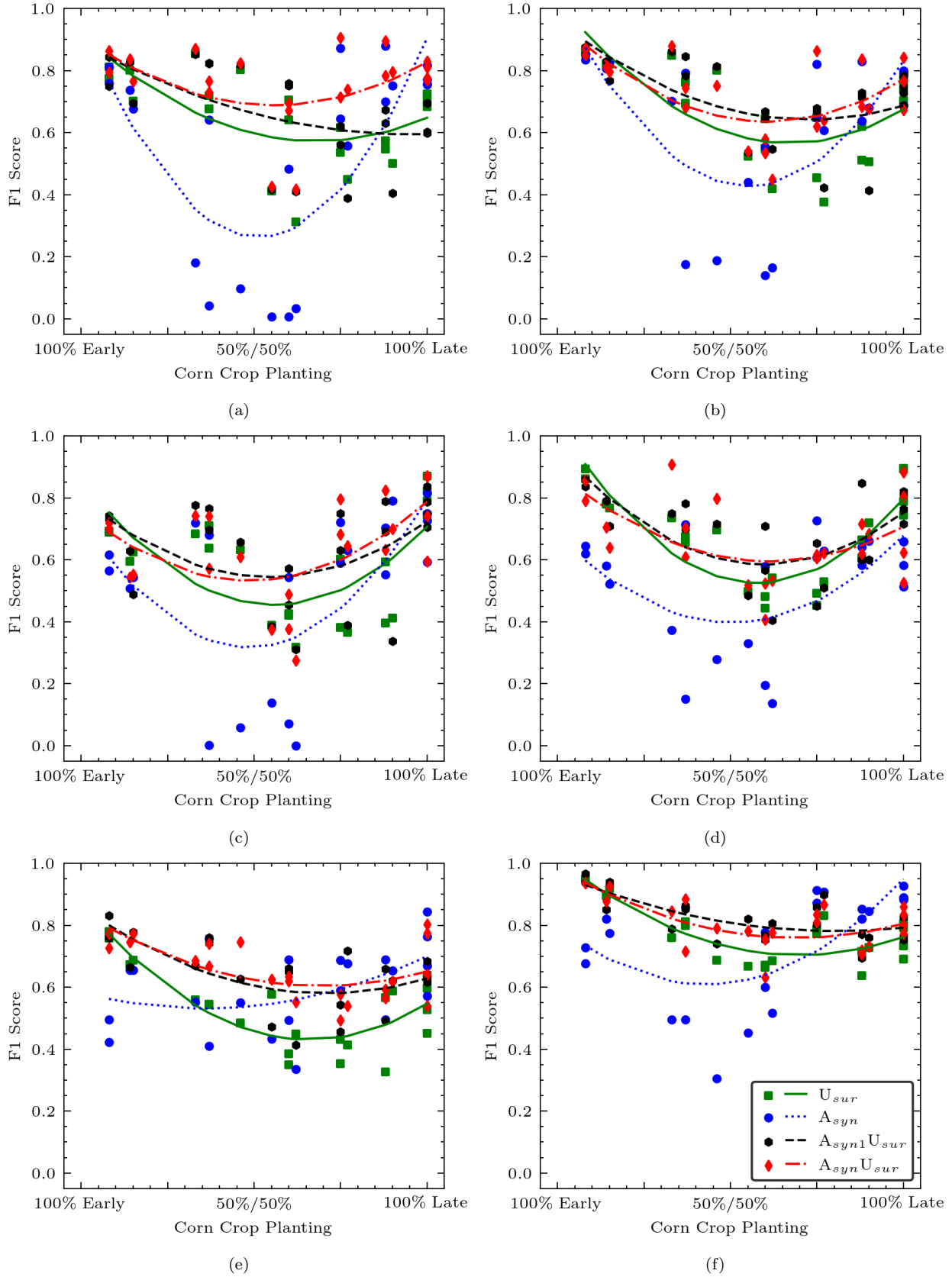


Figure 10:  $F_1$  score for the 2019/20 and 2020/21 test seasons in Argentina as a function of the percentage of early and late planted corn for the (a) pre-emergence, (b) emerged, (c) silking, (d) dough, (e) mature, and (f) harvested stages. Lines represent second degree polynomials fit to  $F_1$  scores for each training set.



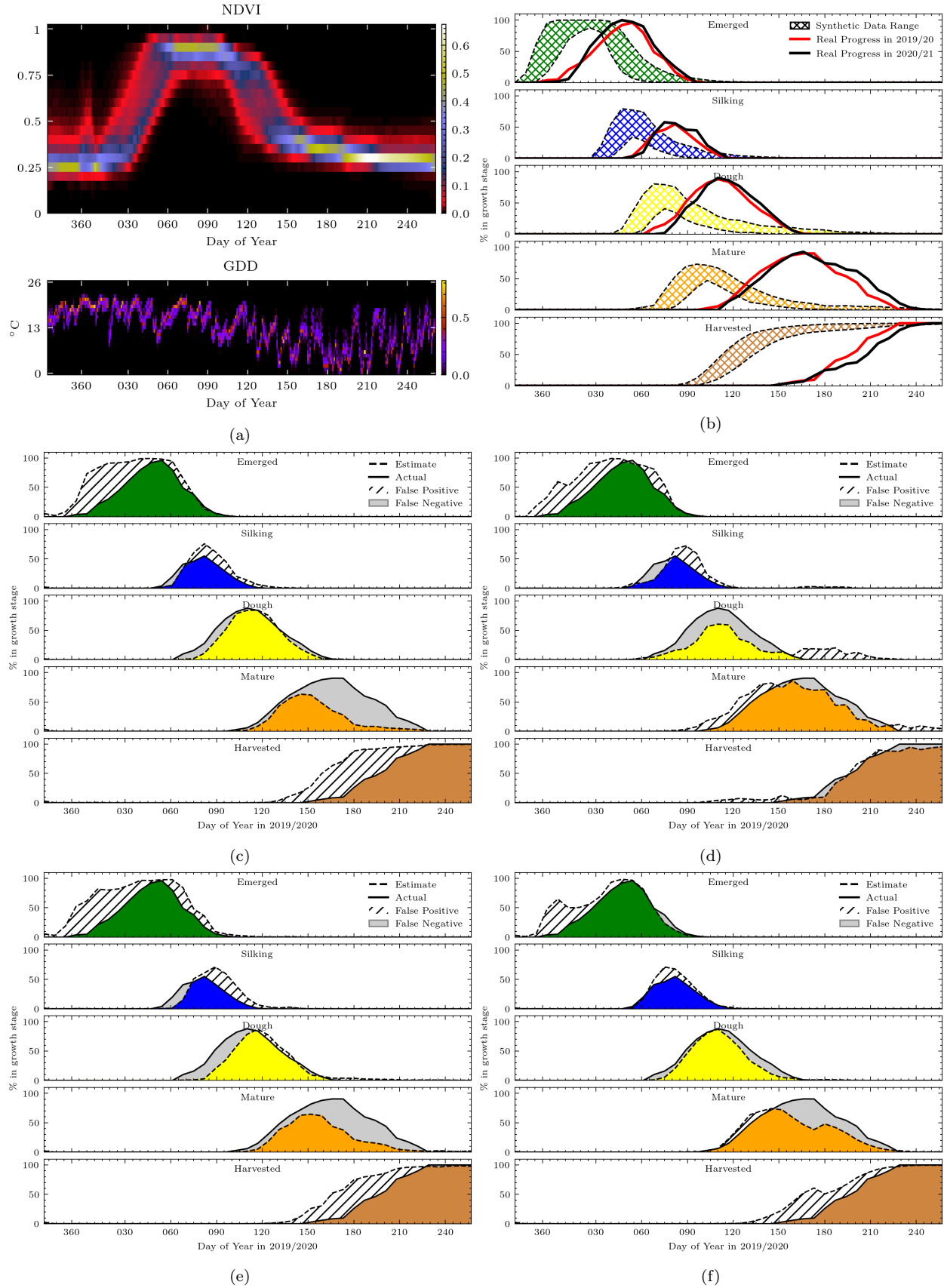


Figure 11: Zone I during the 2019/20 season: (a) NDVI and GDD inputs, (b) test seasons and synthetic data range for crop progress, and crop progress estimates when the network was trained on (c)  $U_{sur}$ , (d)  $A_{syn}$ , (e)  $A_{syn}U_{sur}$ , and (f)  $A_{syn}U_{sur}$ .

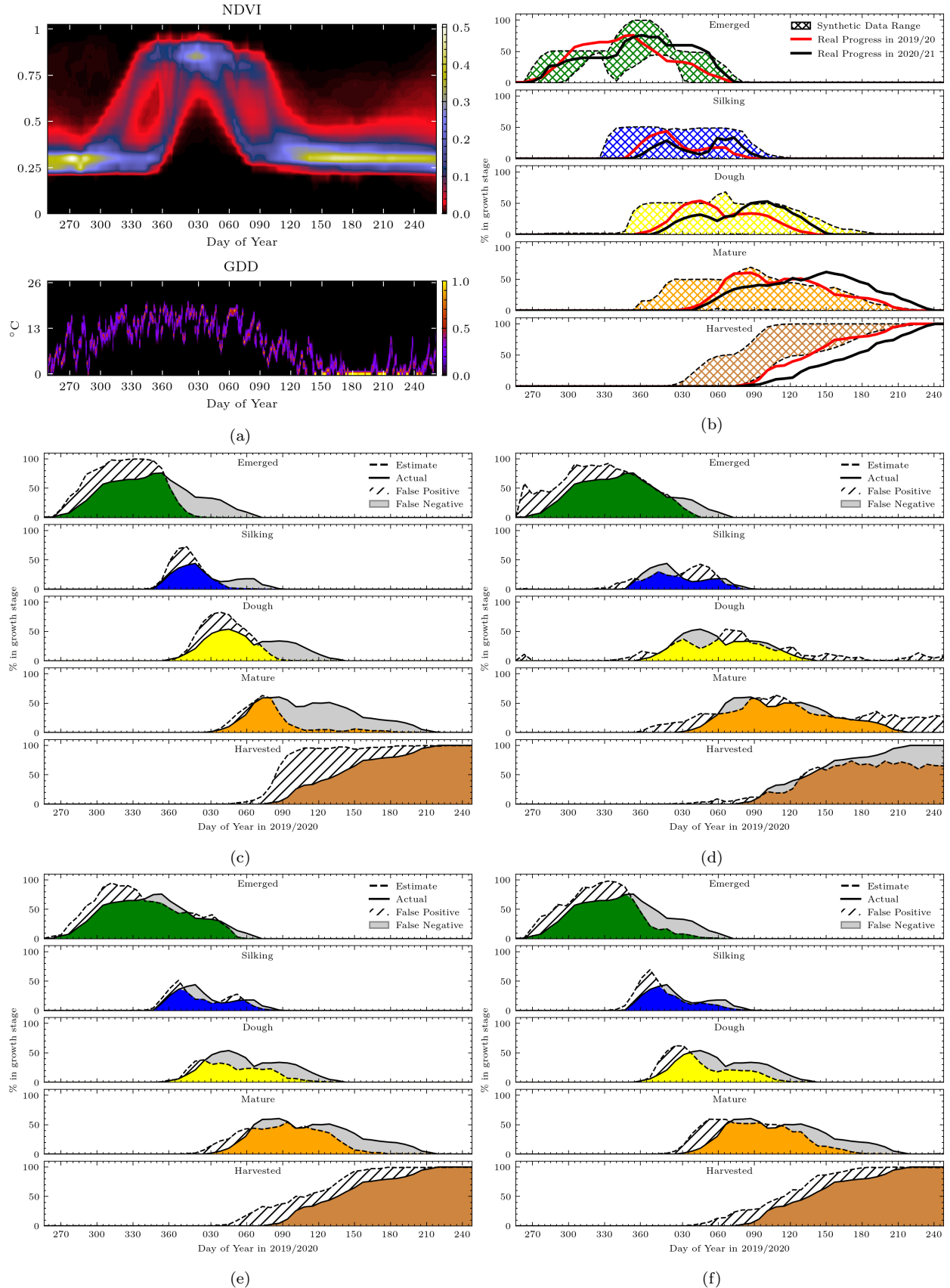


Figure 12: Zone IX during the 2019/20 season: (a) NDVI and GDD inputs, (b) test seasons and synthetic data range for crop progress, and crop progress estimates when the network was trained on (c)  $U_{sur}$ , (d)  $A_{syn}$ , (e)  $A_{syn}U_{sur}$ , and (f)  $A_{syn}U_{sur}$ .

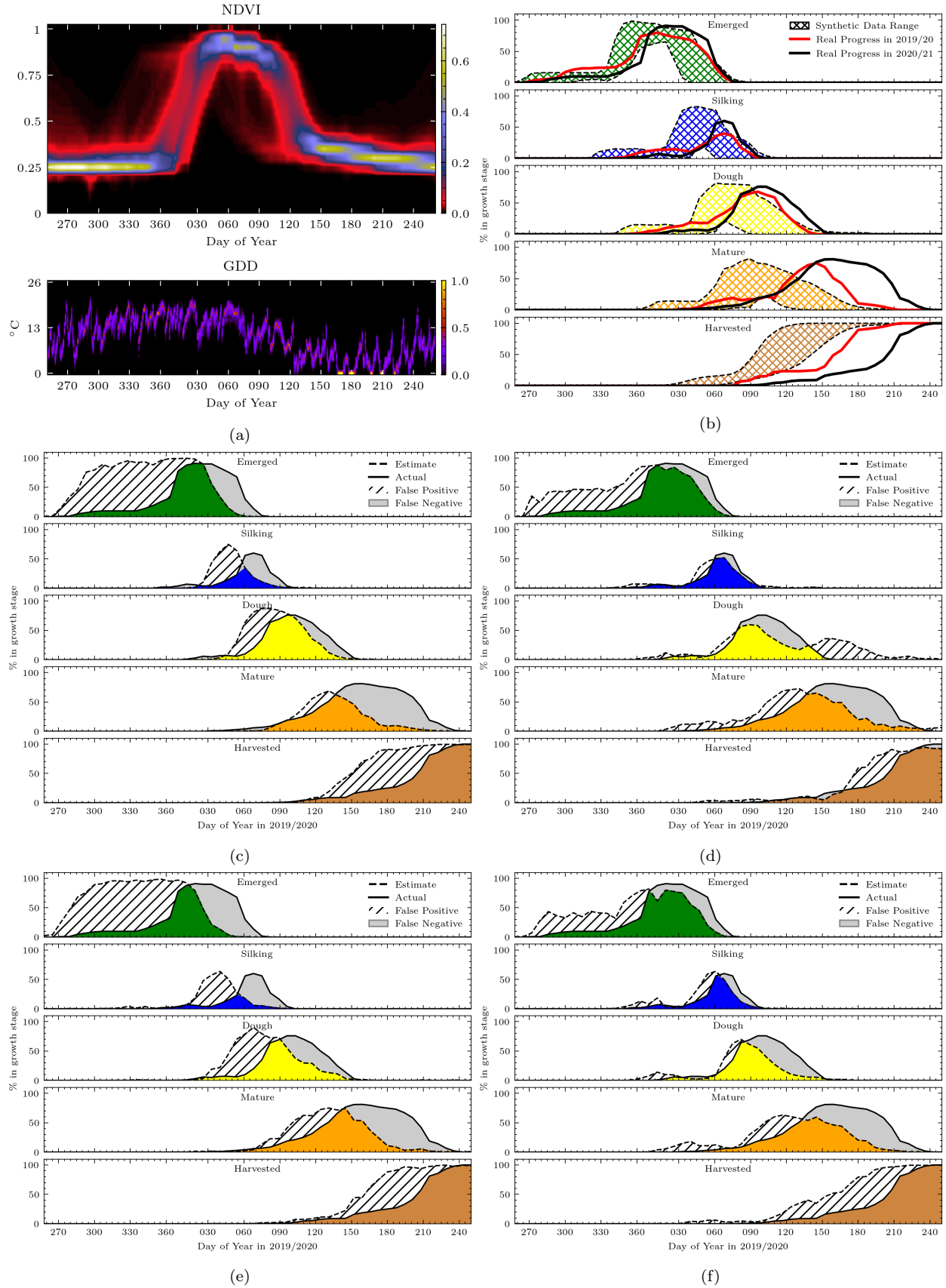


Figure 13: Zone III during the 2020/21 season: (a) NDVI and GDD inputs, (b) test seasons and synthetic data range for crop progress, and crop progress estimates when the network was trained on (c)  $U_{sur}$ , (d)  $A_{syn}$ , (e)  $A_{syn}U_{sur}$ , and (f)  $A_{syn}U_{sur}$ .

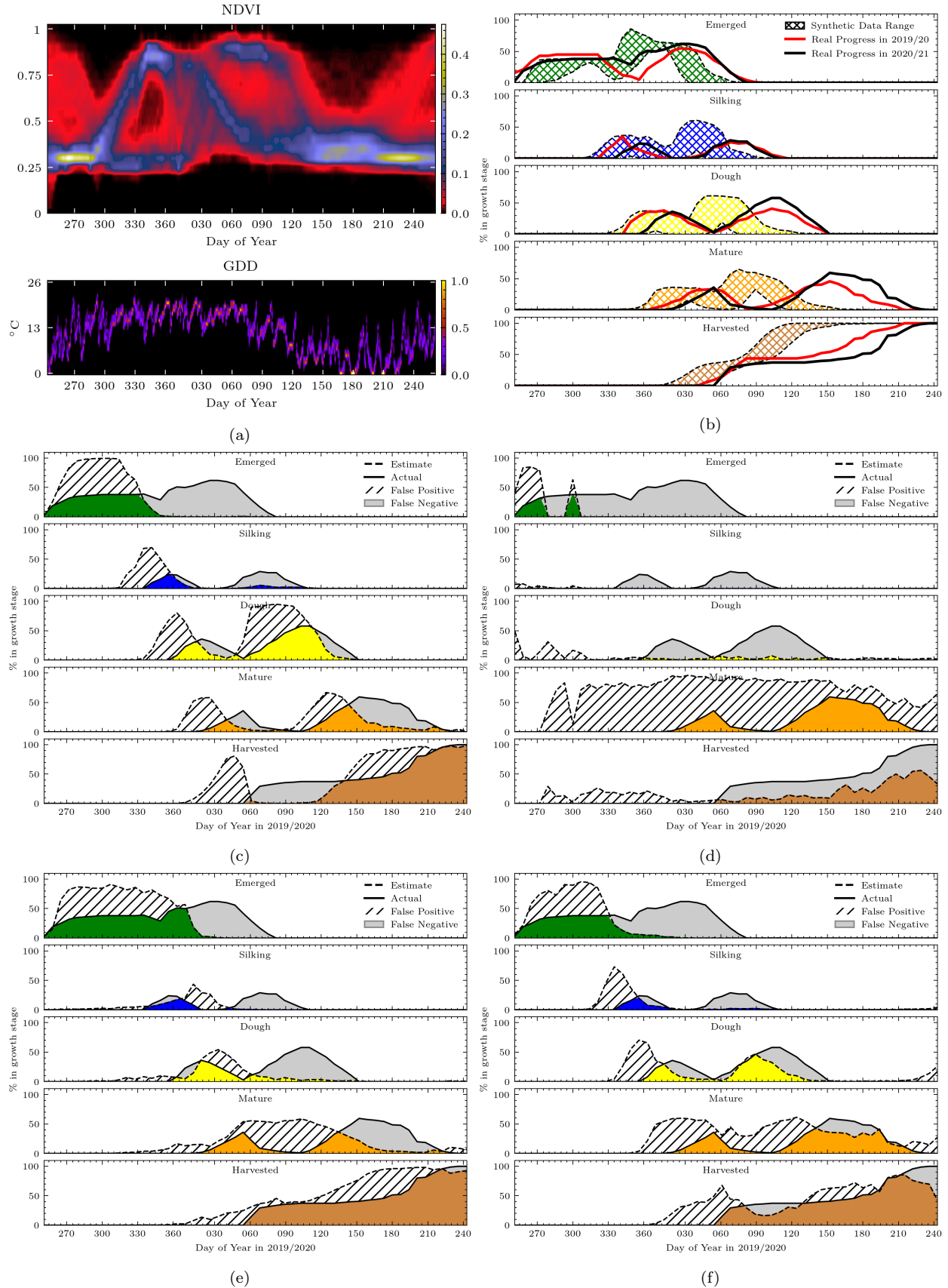


Figure 14: Zone V during the 2020/21 season: (a) NDVI and GDD inputs, (b) test seasons and synthetic data range for crop progress, and crop progress estimates when the network was trained on (c)  $U_{sur}$ , (d)  $A_{syn}$ , (e)  $A_{syn}U_{sur}$ , and (f)  $A_{syn}U_{sur}$ .

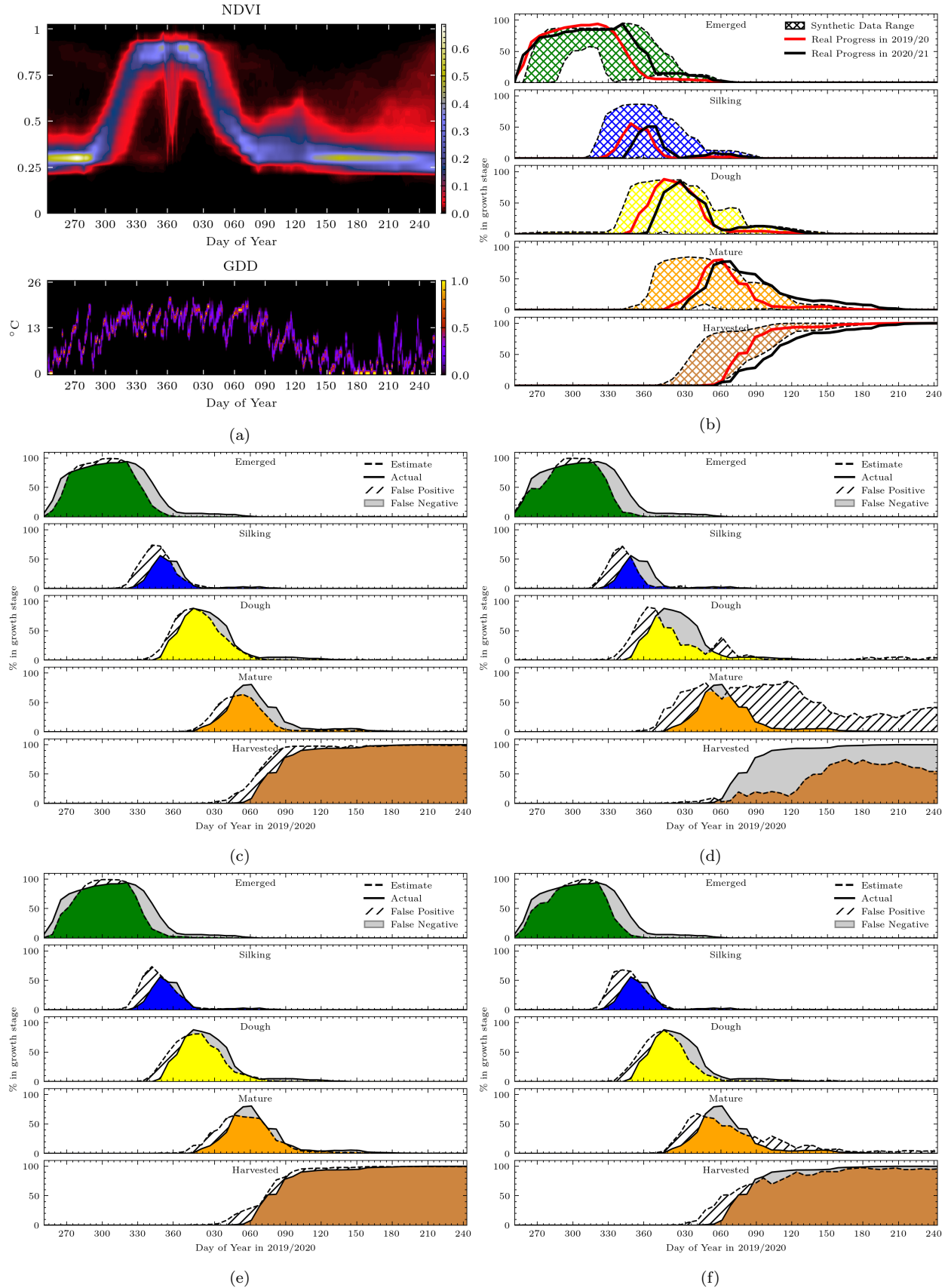
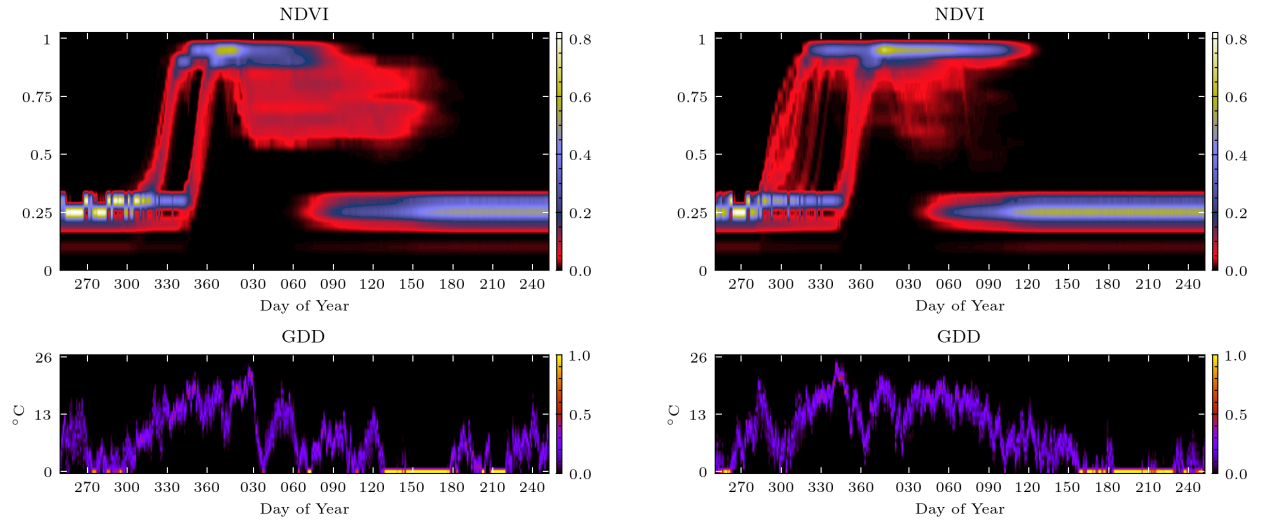
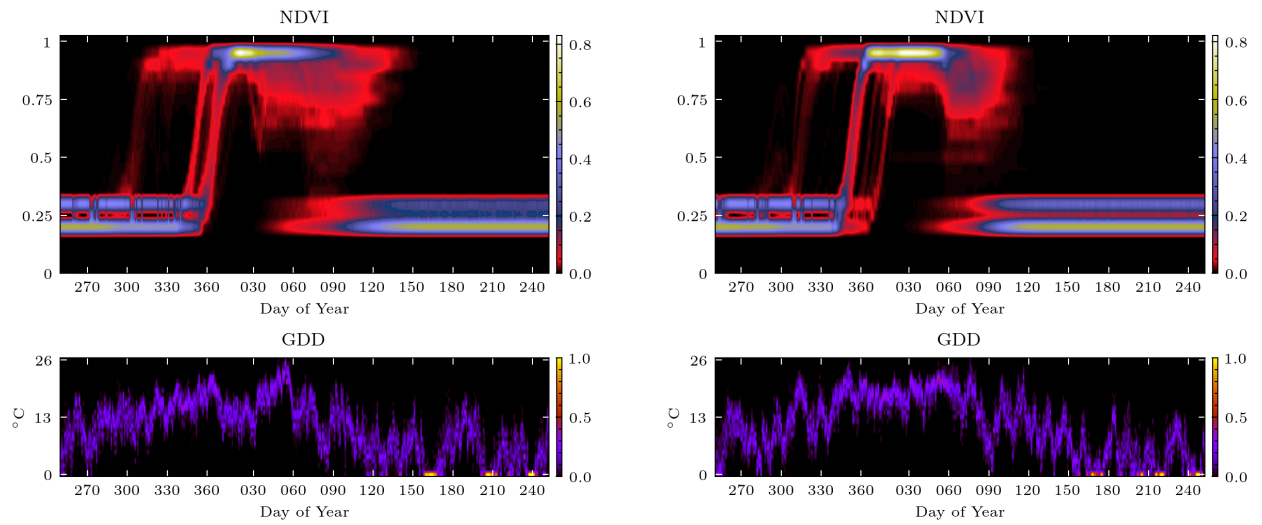


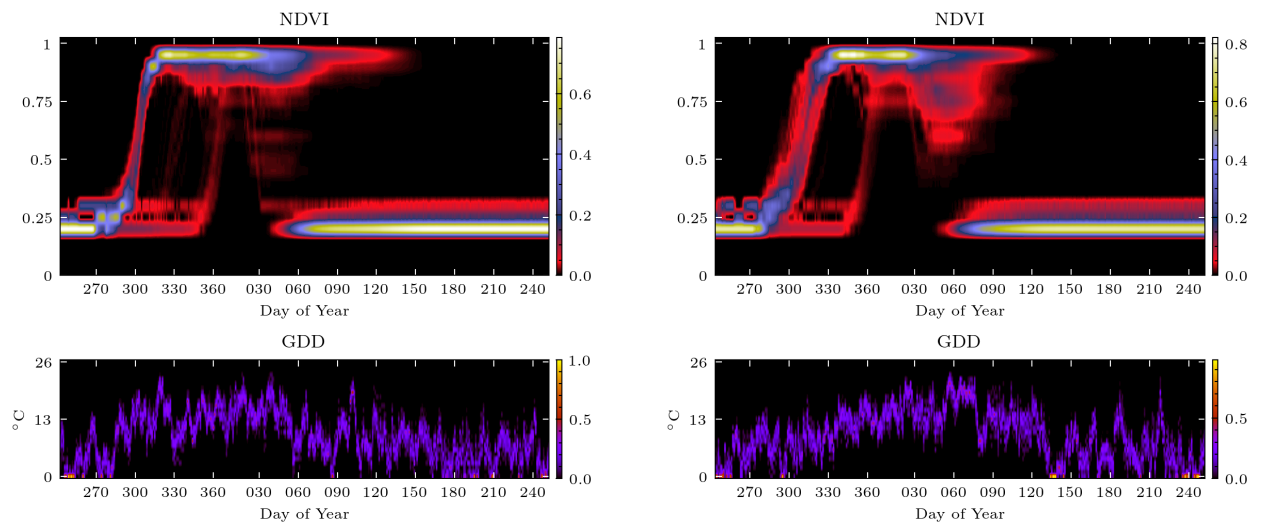
Figure 15: Zone VI during the 2019/20 season: (a) NDVI and GDD inputs, (b) test seasons and synthetic data range for crop progress, and crop progress estimates when the network was trained on (c)  $U_{sur}$ , (d)  $A_{syn}$ , (e)  $A_{syn}U_{sur}$ , and (f)  $A_{syn}U_{sur}$ .



(a)



(b)



(c)

Figure 16: Example synthetic NDVI and GDD histograms generated by the linked SWG-IXIM-SPART models for Zones (a) IX, (b), III, and (c) VI.

## 7. Tables

Table 1: Distribution of corn between early and late planting windows within zones in Argentina.

Zone	2019/20		2020/21		Four Year Average	
	Early Planting	Late Planting	Early Planting	Late Planting	Early Planting	Late Planting
I	-	100%	-	100%	-	100%
II	-	100%	-	100%	-	100%
III	23%	77%	10%	90%	16%	84%
IV	25%	75%	12%	88%	19%	81%
V	45%	55%	38%	62%	38%	62%
VI	92%	8%	85%	15%	87%	13%
VII	92%	8%	86%	14%	86%	14%
IX	63%	37%	40%	60%	51%	49%
X	63%	37%	40%	60%	47%	53%
XII	67%	33%	54%	46%	59%	41%
XIII	25%	75%	12%	88%	19%	81%

Table 2: Sources, resolutions, and pre-processing of inputs to NN-based in-season CPE method

Input	Source	Spat. Resolution	Temp. Resolution	Pre-processing	Reference
NDVI	MODIS Aqua	250 m	7 days	linear interpolation - binned histogram	(Jenkerson et al., 2010)
Growing Degree Days	NASA POWER	$0.5^\circ \times 0.625^\circ$	Daily	binned histogram	(NASA Langley Research Center)



Table 3: Synthetic data generation inputs for the SWG, IXIM, and SPART models

Parameter	Name	Unit	Value / Source
SWG			
TMAX	Daily Maximum Temperature	°C	NASA Langley Research Center
TMIN	Daily Minimum Temperature	°C	NASA Langley Research Center
SRAD	Daily Total Solar Radiation	W/m <sup>2</sup> /day	NASA Langley Research Center
PPT	Daily precipitation	mm/day	NASA Langley Research Center
DSSAT IXIM			
TMAX	Daily Maximum Temperature	°C	Stochastic Weather Generator
TMIN	Daily Minimum Temperature	°C	Stochastic Weather Generator
SRAD	Daily Total Solar Radiation	W/m <sup>2</sup> /day	Stochastic Weather Generator
PPT	Daily precipitation	mm/day	Stochastic Weather Generator
Cultivar	Corn cultivar parameters	-	Andrés Ferreyra et al. (2001)
Soil	Soil properties	-	Han et al. (2019)
SPART			
-	Dry soil reflectance	-	Meerdink et al. (2019)
SM <sub>p</sub>	Soil moisture volume (%)	-	DSSAT simulation
C <sub>ab</sub>	Chlorophyll a + b content	μg cm <sup>-2</sup>	40
C <sub>dm</sub>	Leaf mass per unit area	g cm <sup>-2</sup>	0.01
C <sub>w</sub>	Equivalent water thickness	cm	0.02
C <sub>s</sub>	Brown pigments	-	0
C <sub>ant</sub>	Anthocyanin content	μg cm <sup>-2</sup>	10
N	Leaf structure parameter	-	1.5
LAI	Leaf area index	m <sup>2</sup> m <sup>-2</sup>	DSSAT simulation
LIDF	Leaf inclination distribution function	-	Judge et al. (2021)
q	hot spot parameter	-	Judge et al. (2021)

Table 4: Comparison of USDA, BdC, and study-defined growth stages

Target Stages	BdC Stages	USDA Stages
Emerged	Expansión foliar	Emerged
	Panojamiento	
Silking	Floración Femenina	Silking
Dough	Grano Pastoso	Dough
		Dent
Mature	Madurez Fisiológica	Mature
Harvested	Cosecha	Harvested

Table 5: Net  $F_1$  scores for each training dataset in all zones in Argentina across the 2019/2020 and 2020/2021 test seasons. Bold values indicate the highest net  $F_1$  score for each stage. Values in italics represent the scores for the SRR training set tested in Iowa during the 2018, 2019, and 2020 growing seasons.

Training Set	Preemergence	Emerged	Silking	Dough	Mature	Harvested	Overall
$U_{sur}$	0.632	0.667	0.582	0.667	0.529	0.786	0.677
$A_{syn}$	0.586	0.661	0.574	0.480	0.567	0.755	0.618
$A_{syn1}U_{sur}$	0.656	0.706	0.633	<b>0.690</b>	0.639	<b>0.834</b>	0.723
$A_{syn}U_{sur}$	<b>0.764</b>	<b>0.721</b>	<b>0.641</b>	0.668	<b>0.657</b>	0.822	<b>0.736</b>
SRR (Iowa)	<i>0.900</i>	<i>0.913</i>	<i>0.875</i>	<i>0.909</i>	<i>0.846</i>	<i>0.917</i>	<i>0.898</i>

Table 6:  $F_1$  score of each training method for all zones in Argentina in 2019/20. Bold values indicate the highest  $F_1$  score for each stage within each zone.  $Net_S$  and  $Net_Z$  represent net  $F_1$  scores by stage and zone, respectively.

Zone	$U_{sur}$						$A_{syn}U_{sur}$						$Net_S$
	Pre-emergence	Emerged	Silking	Dough	Mature	Harvested	Pre-emergence	Emerged	Silking	Dough	Mature	Harvested	
I	0.684	0.771	0.791	<b>0.894</b>	0.640	0.793	0.694	0.748	0.706	0.821	0.684	0.828	0.759
II	0.718	<b>0.704</b>	0.744	<b>0.744</b>	0.527	0.806	0.602	0.687	<b>0.746</b>	0.716	<b>0.617</b>	0.826	0.717
III	0.450	0.377	0.366	0.530	0.413	0.832	0.389	0.422	0.389	0.510	<b>0.718</b>	0.899	0.605
IV	0.536	0.454	0.381	0.453	0.431	0.787	0.562	<b>0.679</b>	<b>0.749</b>	<b>0.654</b>	0.544	0.858	0.700
V	0.412	0.523	<b>0.389</b>	0.498	0.578	0.667	0.417	0.536	0.386	0.485	0.473	<b>0.821</b>	0.606
VI	0.775	<b>0.860</b>	0.690	<b>0.861</b>	0.758	0.951	0.750	0.850	<b>0.743</b>	0.837	<b>0.831</b>	<b>0.967</b>	<b>0.889</b>
VII	0.811	0.867	0.692	<b>0.894</b>	<b>0.780</b>	<b>0.947</b>	0.844	<b>0.876</b>	<b>0.731</b>	0.860	0.760	0.938	0.876
IX	0.677	0.694	0.710	0.675	0.543	0.811	<b>0.822</b>	<b>0.845</b>	<b>0.765</b>	0.699	0.743	0.863	<b>0.815</b>
X	0.720	0.762	0.638	0.657	0.546	0.800	<b>0.825</b>	<b>0.783</b>	0.696	<b>0.781</b>	<b>0.760</b>	<b>0.853</b>	<b>0.803</b>
XII	0.854	0.849	0.683	0.735	0.559	0.761	0.852	0.862	<b>0.776</b>	0.749	<b>0.670</b>	0.789	0.792
XIII	0.616	0.649	0.602	0.491	0.354	0.772	0.620	0.670	0.630	0.451	0.457	0.803	0.662
Netz	0.641	0.684	0.607	0.668	0.557	0.822	0.661	0.722	0.664	0.692	<b>0.662</b>	<b>0.867</b>	0.711
	$A_{syn}$												
	$A_{syn}U_{sur}$												
I	0.754	0.783	0.727	0.659	<b>0.844</b>	<b>0.927</b>	0.803	<b>0.842</b>	<b>0.870</b>	0.883	0.802	0.859	<b>0.845</b>
II	0.770	0.688	0.593	0.513	0.572	<b>0.883</b>	0.704	0.674	0.595	0.525	0.539	0.799	0.683
III	0.557	0.607	0.631	<b>0.629</b>	0.676	<b>0.907</b>	0.696	<b>0.640</b>	<b>0.645</b>	0.622	0.540	0.866	<b>0.716</b>
IV	0.644	0.649	0.590	0.607	<b>0.687</b>	<b>0.913</b>	<b>0.717</b>	0.619	0.682	0.616	0.578	0.834	0.702
V	0.007	0.440	0.139	0.330	0.433	0.452	0.359	<b>0.540</b>	0.375	<b>0.518</b>	<b>0.625</b>	0.782	<b>0.614</b>
VI	0.758	0.835	0.565	0.620	0.423	0.676	0.641	0.850	0.719	0.791	0.726	0.937	0.857
VII	0.812	0.851	0.616	0.645	0.495	0.728	0.689	0.873	0.699	0.857	0.773	0.938	0.876
IX	0.641	0.792	0.680	<b>0.714</b>	<b>0.756</b>	0.858	0.769	0.745	0.740	0.703	0.741	<b>0.885</b>	0.791
X	0.043	0.176	0.001	0.151	0.410	0.495	0.325	0.681	0.572	0.609	0.667	0.715	0.679
XII	0.181	0.701	0.720	0.373	0.552	0.496	0.488	<b>0.879</b>	0.742	<b>0.907</b>	<b>0.686</b>	<b>0.845</b>	<b>0.831</b>
XIII	0.872	0.821	0.721	<b>0.727</b>	<b>0.589</b>	<b>0.873</b>	0.800	<b>0.864</b>	<b>0.796</b>	0.605	0.494	0.810	0.783
Netz	0.579	0.693	0.585	0.502	0.556	0.759	0.606	<b>0.749</b>	<b>0.675</b>	<b>0.699</b>	0.657	0.851	<b>0.729</b>

Table 7: F<sub>1</sub> score of each training method for all zones in Argentina in 2020/21. Bold values indicate the highest F<sub>1</sub> score for each stage within each zone. Net<sub>S</sub> and Net<sub>Z</sub> represent net F<sub>1</sub> scores by stage and zone, respectively.

Zone	U <sub>sur</sub>							A <sub>syn</sub> U <sub>sur</sub>						
	Pre-emergence	Emerged	Silking	Dough	Mature	Harvested	Net <sub>S</sub>	Pre-emergence	Emerged	Silking	Dough	Mature	Harvested	Net <sub>S</sub>
I	0.700	0.765	<b>0.870</b>	<b>0.896</b>	0.597	0.733	0.746	0.695	0.783	0.786	0.812	0.627	0.753	0.740
II	0.724	0.739	0.822	<b>0.789</b>	0.451	0.691	0.691	0.598	0.728	<b>0.836</b>	0.764	0.632	0.763	0.715
III	0.501	0.506	0.412	<b>0.720</b>	0.588	0.729	0.590	0.404	0.414	0.337	0.601	0.621	0.760	0.544
IV	0.547	0.511	0.396	0.664	0.566	0.716	0.587	0.630	<b>0.714</b>	<b>0.788</b>	<b>0.848</b>	0.659	0.770	<b>0.722</b>
V	0.313	0.419	<b>0.318</b>	<b>0.542</b>	0.450	0.685	0.508	0.410	<b>0.547</b>	0.311	0.405	0.414	<b>0.807</b>	<b>0.568</b>
VI	0.701	0.821	<b>0.626</b>	<b>0.768</b>	0.688	0.919	<b>0.821</b>	0.695	0.768	0.489	0.709	<b>0.778</b>	<b>0.940</b>	0.811
VII	0.801	0.822	0.595	0.779	0.674	<b>0.896</b>	<b>0.814</b>	0.828	<b>0.829</b>	<b>0.629</b>	<b>0.790</b>	0.664	0.851	0.797
IX	0.642	0.548	0.426	0.443	0.350	0.671	0.556	<b>0.751</b>	<b>0.667</b>	<b>0.572</b>	0.566	0.661	0.753	<b>0.689</b>
X	0.706	0.645	0.420	0.482	0.385	0.664	0.594	<b>0.758</b>	<b>0.647</b>	<b>0.455</b>	<b>0.708</b>	<b>0.650</b>	<b>0.767</b>	<b>0.695</b>
XII	0.803	0.801	0.632	0.697	0.484	0.687	0.700	0.818	<b>0.814</b>	<b>0.658</b>	0.715	0.627	0.741	0.742
XIII	0.574	0.620	0.594	0.605	0.326	0.638	0.572	0.674	0.728	0.691	0.601	0.492	0.694	0.659
Net <sub>Z</sub>	0.623	0.651	0.557	0.666	0.504	0.744	0.626	0.652	0.691	0.600	<b>0.688</b>	0.619	<b>0.794</b>	0.673

Zone	U <sub>syn</sub>							A <sub>syn</sub> U <sub>syn</sub>						
	Pre-emergence	Emerged	Silking	Dough	Mature	Harvested	Net <sub>S</sub>	Pre-emergence	Emerged	Silking	Dough	Mature	Harvested	Net <sub>S</sub>
I	0.756	<b>0.799</b>	0.816	0.659	0.763	<b>0.890</b>	0.784	<b>0.769</b>	0.768	0.869	0.805	<b>0.775</b>	0.835	<b>0.798</b>
II	<b>0.817</b>	<b>0.793</b>	0.750	0.583	<b>0.670</b>	<b>0.889</b>	<b>0.752</b>	0.810	0.765	0.740	0.623	0.642	0.773	0.725
III	0.751	<b>0.681</b>	<b>0.790</b>	0.661	<b>0.653</b>	<b>0.846</b>	<b>0.725</b>	<b>0.795</b>	0.676	0.700	0.683	0.618	0.731	0.707
IV	0.699	0.638	0.552	0.582	<b>0.690</b>	<b>0.852</b>	0.685	<b>0.783</b>	0.683	0.632	0.620	0.594	0.707	0.682
V	0.033	0.165	0.000	0.137	0.335	0.517	0.294	<b>0.417</b>	0.449	0.275	0.533	<b>0.553</b>	0.777	0.565
VI	0.677	<b>0.827</b>	0.544	0.522	0.656	0.775	0.711	<b>0.766</b>	0.795	0.553	0.640	0.773	0.926	0.811
VII	0.737	0.806	0.507	0.581	0.656	0.820	0.731	<b>0.837</b>	0.810	0.544	0.706	<b>0.746</b>	0.878	0.801
IX	0.483	0.554	0.544	<b>0.579</b>	<b>0.689</b>	<b>0.778</b>	0.625	0.694	0.579	0.488	0.523	0.620	0.754	0.644
X	0.007	0.140	0.070	0.195	0.494	0.600	0.345	0.671	0.535	0.376	0.407	0.634	0.633	0.575
XII	0.098	0.188	0.058	0.279	0.551	0.306	0.318	<b>0.825</b>	0.751	0.610	<b>0.797</b>	<b>0.746</b>	<b>0.791</b>	<b>0.769</b>
XIII	0.879	0.830	0.704	0.641	0.496	<b>0.821</b>	0.750	<b>0.896</b>	<b>0.836</b>	<b>0.824</b>	<b>0.716</b>	<b>0.564</b>	0.719	<b>0.762</b>
Net <sub>Z</sub>	0.592	0.629	0.561	0.460	0.567	0.750	0.573	<b>0.760</b>	<b>0.694</b>	<b>0.605</b>	0.639	<b>0.657</b>	0.787	<b>0.687</b>